



**POLITECNICO**  
MILANO 1863

SCUOLA DI INGEGNERIA INDUSTRIALE  
E DELL'INFORMAZIONE

# Deep-Learning-based segmentation of the aorta from dynamic 2D Magnetic Resonance Images

TESI DI LAUREA MAGISTRALE IN  
BIOMEDICAL ENGINEERING - INGEGNERIA BIOMEDICA

Author: **Célia Muriel Emilie Jaffré**

Student ID: 986034

Advisor: Prof. Elena De Momi

Co-advisors: Thomas Dietenbeck, Nadjia Kachenoura

Academic Year: 2022-2023



# Abstract

Aortic stiffness is a relevant indicator of cardiovascular pathology, and its measurement plays a crucial role in diagnosing disease conditions and predicting patients outcomes. However, accurately segmenting the aorta from 2D dynamic Magnetic Resonance Imaging (MRI) images using traditional image processing poses significant challenges being time consuming and subject to operator variability. This thesis presents a novel approach for the automated segmentation of the aortic lumen from dynamic velocity encoded 2D MRI images, using deep learning techniques and specifically the UNet++ architecture. This architecture, known for its ability to capture fine-grained details and effectively handle semantic segmentation tasks, serves as the foundation for the developed model. The architecture incorporates skip connections and dense connections to enable the efficient extraction of features at multiple scales. Several algorithms have been developed: a vanilla UNet++ taking the entire image as an input, a second UNet++ taking the image cropped on a Region of Interest (ROI) surrounding both the ascending (AAo) and the descending (DAo) aorta; and two UNet++ taking as input two independent ROIs corresponding to the AAo or the DAo. Extensive experiments were conducted to fine-tune hyperparameters and assess the impact of different training configurations on the model's performance.

The results of the experiments, achieved on a database of 403 patients, demonstrated the effectiveness of the Vanilla method and the AAo and DAo-centered method in accurately segmenting the aorta from 2D dynamic MRI images. Both methods achieved a high Dice coefficient higher than 0.97 and low Hausdorff distances smaller than 2 pixels, indicating a strong agreement between the prediction and the ground truth segmentations. In conclusion, this thesis presents a novel approach for the segmentation of the aorta on 2D dynamic MRI images using the UNet++ architecture. The developed model exhibits promising results and therefore has the potential to aid clinicians in accurate and fully automated aortic segmentation, thus facilitating the diagnosis and treatment of cardiovascular diseases.

**Keywords:** Aortic stiffness, 2D dynamic MRI, Segmentation, Deep Learning, UNet++



# Sommario

La rigidità aortica è un indicatore rilevante della patologia cardiovascolare e la sua misurazione svolge un ruolo cruciale nella diagnosi delle condizioni patologiche e nella previsione degli esiti dei pazienti. Tuttavia, l'accurata segmentazione dell'aorta da immagini di Risonanza Magnetica (RM) dinamica 2D mediante l'elaborazione tradizionale delle immagini pone sfide significative in quanto richiede tempo ed è soggetta alla variabilità dell'operatore. Questa tesi presenta un approccio innovativo per la segmentazione automatica del lume aortico da immagini di RM 2D con codifica della velocità dinamica, utilizzando tecniche di Deep Learning (DL) e in particolare l'architettura UNet++. Questa architettura, nota per la sua capacità di catturare dettagli a grana fine e di gestire efficacemente compiti di segmentazione semantica, funge da base per il modello sviluppato. L'architettura incorpora connessioni saltate e dense per consentire l'estrazione efficiente di caratteristiche a più scale. Sono stati sviluppati diversi algoritmi: un UNet++ vanilla che prende in input l'intera immagine, un secondo UNet++ che prende in input l'immagine ritagliata su una regione d'interesse (ROI) che circonda sia l'aorta ascendente (AAo) che quella discendente (DAo); e due UNet++ che prendono in input due ROI indipendenti corrispondenti all'AAo o alla DAo. Sono stati condotti esperimenti approfonditi per mettere a punto gli iperparametri e valutare l'impatto di diverse configurazioni di addestramento sulle prestazioni del modello.

I risultati degli esperimenti, ottenuti su un database di 403 pazienti, hanno dimostrato l'efficacia del metodo Vanilla e del metodo centrato su AAo e DAo nel segmentare accuratamente l'aorta da immagini RM dinamiche 2D. Entrambi i metodi hanno ottenuto un coefficiente Dice elevato, superiore a 0.97, e distanze di Hausdorff ridotte, inferiori a 2 pixel, indicando una forte concordanza tra le segmentazioni previste e quelle reali. In conclusione, questa tesi presenta un nuovo approccio per la segmentazione dell'aorta su immagini di RM dinamica 2D utilizzando l'architettura UNet++. Il modello sviluppato mostra risultati promettenti e ha quindi il potenziale per aiutare i medici nella segmentazione accurata e completamente automatizzata dell'aorta, facilitando così la diagnosi e il trattamento delle malattie cardiovascolari.

**Parole chiave:** Rigidità aortica, RM dinamica 2D, Segmentazione, DL, UNet++



# Contents

<b>Abstract</b>	<b>i</b>
<b>Sommario</b>	<b>iii</b>
<b>Contents</b>	<b>v</b>
<b>1 Introduction</b>	<b>1</b>
1.1 Medical Context . . . . .	1
1.1.1 Healthcare Context . . . . .	1
1.1.2 Anatomical description . . . . .	2
1.2 Medical Imaging . . . . .	7
1.2.1 Magnetic Resonance Imaging . . . . .	7
1.2.2 MRI Phase Contrast . . . . .	9
1.3 Medical needs . . . . .	11
1.3.1 Importance of aortic stiffness measurement . . . . .	11
1.3.2 Need of an accurate segmentation . . . . .	14
1.4 Aim of the work . . . . .	15
<b>2 Literature Review</b>	<b>17</b>
2.1 Medical Imaging . . . . .	17
2.2 Deep Learning approaches . . . . .	20
2.2.1 Convolutional Neural Networks . . . . .	20
2.2.2 UNet . . . . .	25
2.2.3 Recurrent Neural Networks . . . . .	29
2.2.4 Complex methods based on Deep Learning . . . . .	32
<b>3 Materials and Methods</b>	<b>37</b>
3.1 Dataset . . . . .	37
3.2 Data preprocessing . . . . .	40

3.3	Models . . . . .	42
3.3.1	Vanilla Method . . . . .	42
3.3.2	ROI-centered Method . . . . .	43
3.3.3	Ascending Aorta and Descending Aorta-centered Method . . . . .	44
3.4	Metrics Used . . . . .	46
3.4.1	Cross-entropy Loss . . . . .	46
3.4.2	Dice . . . . .	47
3.4.3	Hausdorff . . . . .	48
3.4.4	Mean Absolute Error and Mean Squared Error . . . . .	50
<b>4</b>	<b>Results</b>	<b>51</b>
4.1	Results . . . . .	51
4.2	Results according to the size of the Ascending Aorta . . . . .	55
4.3	Results according to the blood flow velocity computation . . . . .	59
4.4	Effects of Manufacturer and magnetic field strength . . . . .	63
<b>5</b>	<b>Discussion</b>	<b>65</b>
<b>6</b>	<b>Conclusion</b>	<b>67</b>
	<b>Bibliography</b>	<b>69</b>
	<b>List of Figures</b>	<b>79</b>
	<b>List of Tables</b>	<b>81</b>
	<b>Acronyms</b>	<b>83</b>
	<b>Acknowledgements</b>	<b>85</b>

# 1 | Introduction

This chapter provides an overview of the medical framework, and highlights the objectives of this thesis. Section 1.1 explains the medical context of this thesis, and shows that an accurate segmentation of the aorta plays a critical role in cardiovascular assessment and patients management. Section 1.2 briefly summarizes MRI functioning, while focusing on velocity encoded images that will be used in this thesis. In Section 1.3, the current need of an accurate segmentation for quantitative analysis of aortic images is highlighted. Finally, the objectives of this work are developed in Section 1.4.

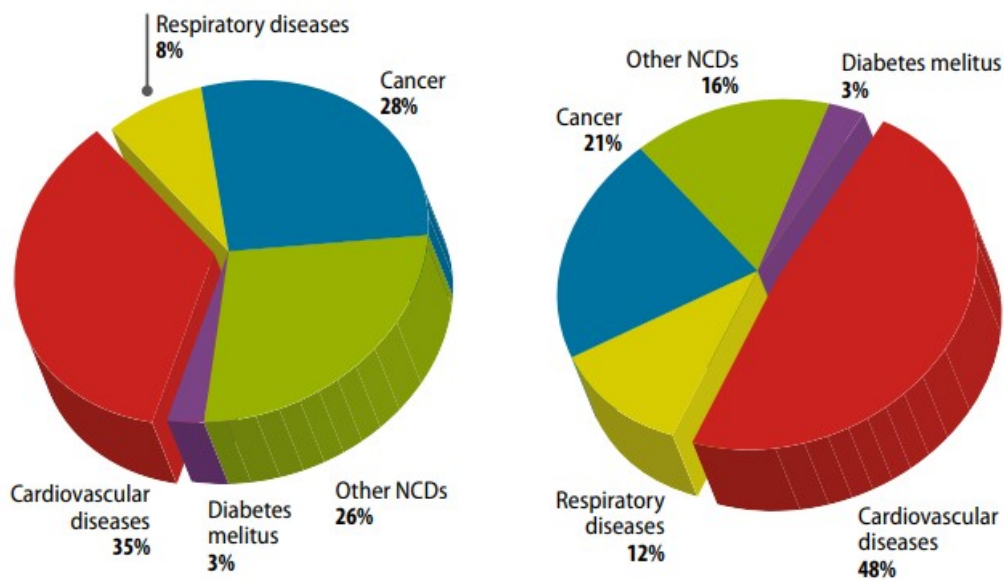
## 1.1. Medical Context

### 1.1.1. Healthcare Context

Noncommunicable Diseases (NCD) are a leading cause of death worldwide, resulting in a substantial loss of life each year. According to the World Health Organization (WHO), NCDs claim the lives of approximately 41 million people annually. This staggering figure accounts for nearly 71% of all global deaths [63]. NCDs cover a wide range of conditions, including Cardiovascular Diseases (CVD), cancer, chronic respiratory diseases, and diabetes. These diseases are often linked to lifestyle factors such as unhealthy diets, physical inactivity, tobacco use, and excessive alcohol consumption [84]. The growing prevalence of NCDs highlights the urgent need for effective prevention strategies and improved healthcare systems to reduce the burden of these diseases on individuals and societies.

The figures presented below (Fig 1.1) depict the distribution of mortality causes attributed to NCDs. Among these diseases, cardiovascular diseases assume the foremost position as the leading cause of death, their significance are further accentuated with populations' aging [63]. However, it is crucial to emphasize that CVD are preventable, and the implementation of effective prevention and control measures can contribute to the decline in CVD cases and their associated mortality burden. Through targeted interventions, such as promoting healthy lifestyles, encouraging regular physical activity, adopting balanced diets, reducing tobacco and alcohol consumption, managing stress, and ensuring access

to quality healthcare services, the burden of CVD can be mitigated [63, 84]. Preventive measures, including regular health check-ups, early detection of risk factors, and timely medical interventions, play a pivotal role in reducing the incidence and severity of CVD. By promoting prevention strategies and fostering public awareness regarding the importance of cardiovascular health, significant progress can be achieved in curbing the prevalence and impact of CVD on individuals and communities. Consequently, early detection and appropriate management of CVD are fundamental for patients.



(a) Distribution of global NCD by causes of death for less than 60 year old persons. (b) Distribution of global NCD by causes of death in the whole population.

Figure 1.1: Worldwide distribution of global NCD by causes of death, according to age [63]. We can notice that the CVD still represent the most important cause of death in the population and is even greater among the elderly.

### 1.1.2. Anatomical description

In order to understand the data used for this thesis, an explanation of the functioning of the heart is necessary. The heart, a vital organ in the circulatory system, functions as a powerful pump that ensures the continuous circulation of blood throughout the body. It consists of four chambers: two atria and two ventricles [57]. The atria receive deoxygenated blood from the body (right atrium) and oxygenated blood from the lungs (left atrium). The ventricles, located below the atria, are responsible for pumping blood out of the heart. The right ventricle pumps deoxygenated blood to the lungs for oxygenation, while the left ventricle pumps oxygenated blood to the rest of the body [29].

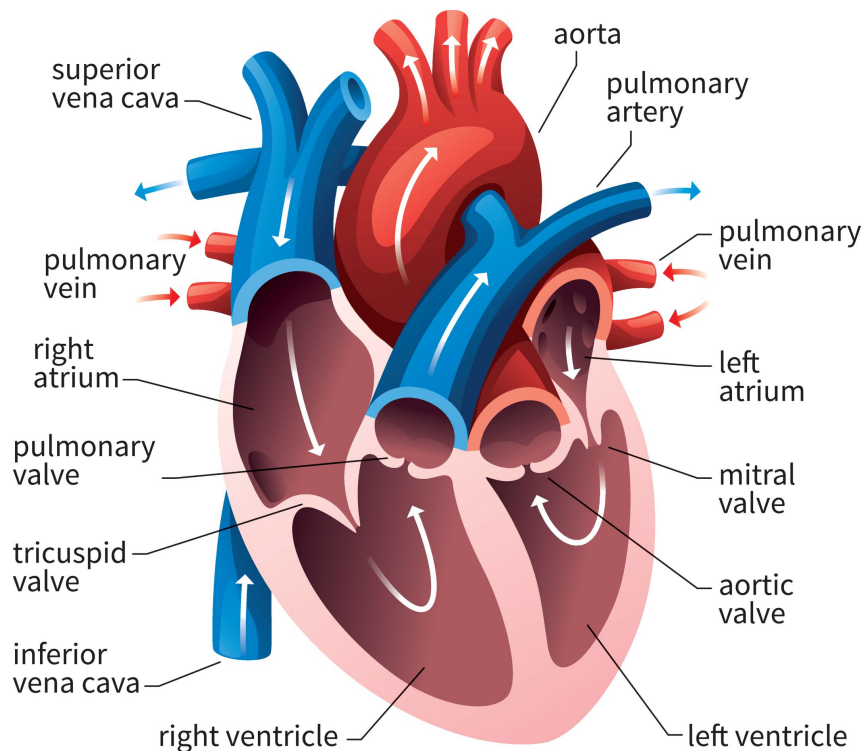
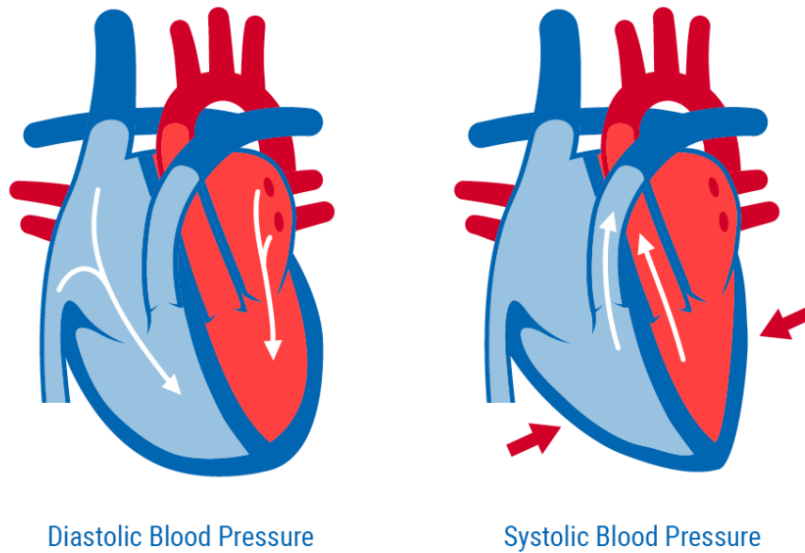


Figure 1.2: Scheme of the blood flow in the human heart, the arrows represent the direction of such flow [3]. Blue stands for the blood with low oxygen content and Red depicts the blood with rich oxygen content.

The heart's coordinated pumping action is regulated by a specialized electrical conduction system. The sinoatrial node, often referred to as the heart's natural pacemaker, initiates the electrical impulses that stimulate the heart muscle (myocardium) to contract. These electrical signals travel through the atria, inducing their contraction to push the blood into the ventricles. The impulses then pass through the atrioventricular node, which briefly delays the signal before transmitting it to the ventricles. This delay allows the atria to fully contract before the ventricles begin their contraction [29]. Once the electrical signal reaches the ventricles, it travels through specialized fibers called bundle branches and Purkinje fibers, rapidly stimulating the ventricles to contract, defining the systolic phase. This coordinated contraction squeezes the blood out of the ventricles, sending it to the lungs or the rest of the body through the respective arteries. The heart's efficient functioning relies on the synchronized contraction and relaxation of its chambers, which is regulated by a complex interplay of electrical signals and mechanical processes. This intricate coordination ensures the continuous blood flow, supplying oxygen and nutrients to the body's tissues and organs [29, 57].

Systole and diastole are two phases of the cardiac cycle that represent the alternating

contraction and relaxation of the heart chambers.



**Figure 1.3:** Representation of the blood pressure during Diastole then Systole in the human heart [4]. The thin (white) arrows represent the blood flow directions and the thicker (red) arrows represent the pressure applied.

During systole, the heart muscles contract, generating pressure that propels blood out of the ventricles. This phase consists of two stages: atrial systole and ventricular systole. Atrial systole occurs first, where the atria contract, fulfilling ventricular filling. This is followed by ventricular systole, during which the ventricles contract forcefully, pushing blood out of the heart into the respective arteries (pulmonary artery and aorta) [66]. Diastole, on the other hand, represents the relaxation and filling phase of the heart chambers. It can also be divided into two stages: early diastole (isovolumetric relaxation) and late diastole (ventricular filling). In early diastole, the ventricles relax and blood flows back from the arteries, causing the semilunar valves (aortic and pulmonary valves) to close. This phase is known as isovolumetric relaxation because the ventricular volume remains constant. This phase is followed by the early ventricular filling phase, during which the ventricles lower their pressure inducing a filling wave flowing from the atria towards the ventricles through the mitral and tricuspid valves, respectively. In late diastole, the atria contract, pushing the remaining blood into the ventricles, completing the filling process [66]. These alternating phases of systole and diastole ensure the efficient pumping of blood by the heart, allowing for the continuous circulation of oxygenated blood to the body and deoxygenated blood to the lungs for oxygenation [29, 57].

The aorta is the largest artery in the human body and plays a crucial role in the circulatory

system. It serves as the main conduit for oxygenated blood pumped out of the left ventricle of the heart to be distributed to the rest of the body.

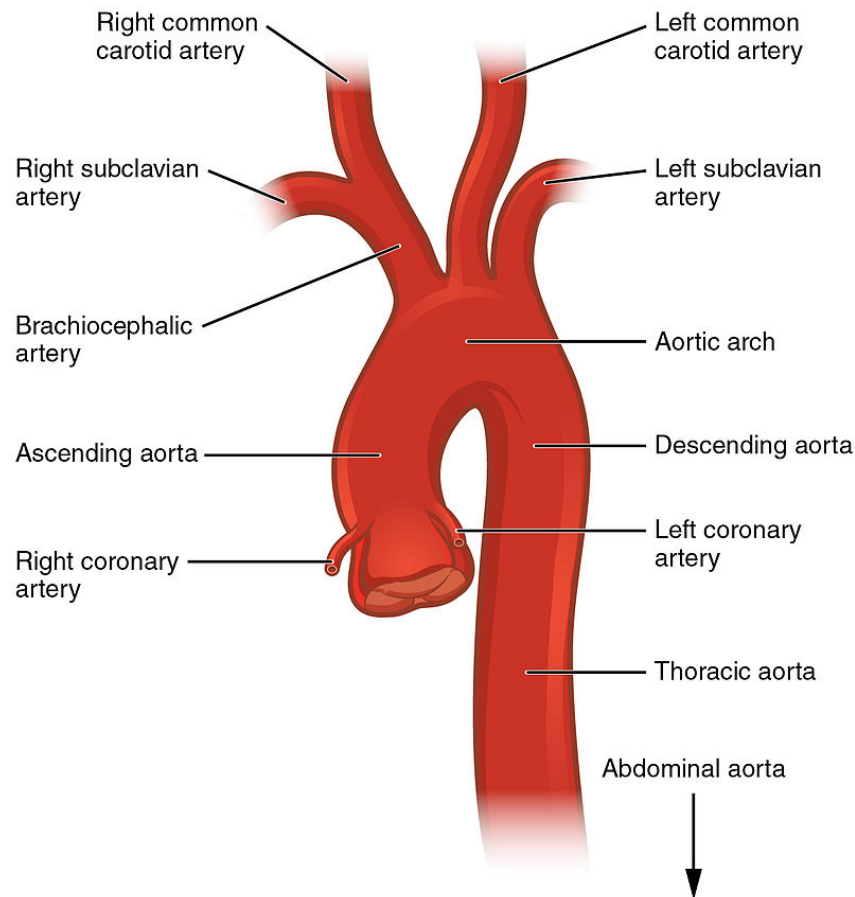


Figure 1.4: Representation of the thoracic section of the Aorta [11]

The primary role of the aorta is to carry oxygen-rich blood ejected by the heart and deliver it to various organs and tissues throughout the body. As the blood leaves the left ventricle during ventricular systole, it enters the aorta through the aortic valve. From there, the aorta branches out into a network of smaller arteries that supply blood to different parts of the body, ensuring a constant flow of oxygen and nutrients to sustain cellular functions.

In addition to its transport function, the aorta also possesses unique structural characteristics that enable it to accommodate the pulsatile nature of blood flow originating from the heart. Its elastic walls allow it to stretch and expand during ventricular systole, absorbing the pressure generated by the heart's contraction. Then its elastic recoil (back to its initial shape after its early systolic expansion) helps propel the blood forward during diastole, maintaining a continuous flow even during the heart relaxation phase.

The aorta is divided into different segments based on its anatomical location, including

the ascending aorta, aortic arch, and descending aorta. Each segment has its own specific roles in directing blood flow to specific regions of the body [29, 57].

The aorta, as a large elastic artery, plays a critical role in dampening the pulsatile pressure generated by the heartbeat, thereby maintaining a relatively steady blood flow to vital organs and tissues, especially the highly vascularized organs such as the brain and the kidneys, which highly need this aortic cushioning. With aging and the presence of certain cardiovascular diseases, the aorta can undergo structural changes that lead to an increase in its stiffness.

When the heart ejects blood into the aorta, a part of the pulse wave travels forward through the arterial system. However, a portion of the pulse wave also reflects back towards the heart when meeting arterial bifurcations or segments with modified stiffness. This phenomenon is known as wave reflection [85].

Wave reflection occurs due to the interaction between the forward-traveling pulse wave and the complex structure of the arterial system, including the branching and elasticity of blood vessels. In a normal condition, the reflected wave returns to the heart during diastole, which is the relaxation phase of the heart to favor myocardial perfusion by pushing the blood present in proximal aorta towards coronary arteries (the vascular network surrounding the heart muscle) [27].

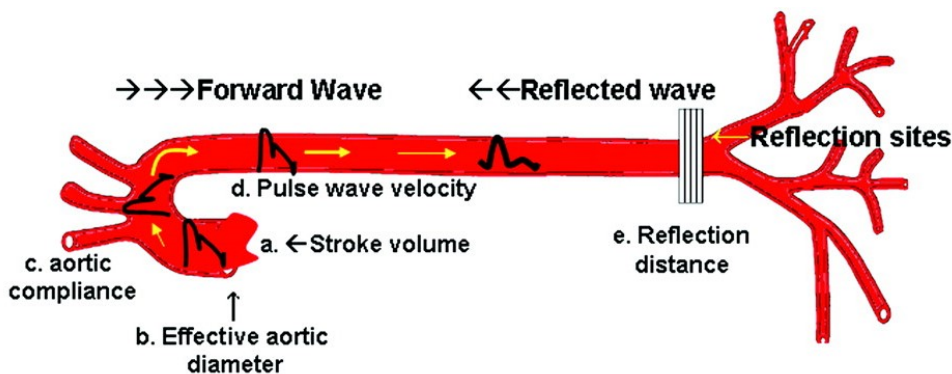


**Figure 1.5:** The Pulse Wave Velocity (PWV) represents the speed at which the pulse wave travels through the arterial tree, determined by arterial wall elasticity or distensibility. As the pulse wave moves, it encounters reflections at the branch points, resulting in backward propagation. The peripheral pulse pressure is the sum of the forward and reflected waves, influenced by factors such as stroke volume, aortic elasticity and diameter, pulse wave velocity, and effective reflecting distance [70]

Additionally, the reflected wave contributes to the regulation of blood pressure and cardiac function. It assists in maintaining optimal blood pressure levels during diastole and

helps to reduce the workload on the heart during systole [85].

During the process of aging or disease the aorta stiffens (loss of its wall elasticity through replacement of its elastin fibers by collagen) inducing a faster PWV and an early return of wave reflection leading simultaneously to a poor myocardial perfusion (low diastolic pressure) and to a deleterious load (high systolic pressure) exerted on the heart during its ejection phase. Such processes highlight the importance of studying and measuring arterial elasticity.

When quantifying global vascular function, the most commonly used technique is tonometry, which provides a global estimation of aortic Pulse Wave Velocity (PWV) between the femoral and carotid artery. However, tonometry fails to account for the often tortuous path of the arteries and relies on body surface measurements to approximate artery length, potentially leading to inaccuracies in PWV estimation, especially in patients with abdominal obesity [24, 25]. The challenges posed by tonometry in accurately quantifying global vascular function have motivated researchers to explore alternative approaches, including the use of medical imaging for quantification.

## 1.2. Medical Imaging

### 1.2.1. Magnetic Resonance Imaging

Magnetic Resonance Imaging (MRI) is a widely used medical imaging technique that allows physicians to obtain detailed images of the internal structures of the human body. It utilizes a powerful magnetic field and radio waves to generate cross-sectional images, providing valuable diagnostic information [68]. MRIs have revolutionized the field of medicine, enabling non-invasive and non-radiating examinations and aiding in the diagnosis and treatment of various medical conditions.



**Figure 1.6:** An MRI machine is composed of a large cylindrical magnet, which creates a strong magnetic field around the patient. It also consists of a patient table that slides into the magnet bore and a radio-frequency system that emits radio waves and detects the signals produced by the body's tissues. The machine is enclosed within a protective Faraday housing and features a control room where technologists operate the scanner and acquire the images [55].

The fundamental principle behind MRI involves the interaction between the body's hydrogen atoms and the magnetic field. When a patient is lying inside the MRI machine, the magnetic field aligns the hydrogen atoms in his body. Radio waves are then emitted, causing the atoms to resonate. As the atoms return to their original state, they emit signals that are detected by specialized receivers. These signals are processed by a computer to generate detailed images [61].

The resulting images produced by MRIs provide precise anatomical detail in terms of contrasts, making it a valuable tool in diagnosing numerous conditions across different medical specialties. MRI scans are particularly useful in assessing soft tissues such as the brain, spinal cord, muscles, ligaments, and organs like the heart, liver, and kidneys. By visualizing these structures, physicians can identify abnormalities, evaluate the extent of injuries, and guide medical treatment and surgical decisions [20].

Moreover, MRI signals can be enhanced with contrast agents to improve the visualization of certain structures or to highlight specific abnormalities. Contrast agents, often based on gadolinium, are administered intravenously and help differentiate between healthy and

diseased tissues, improving the accuracy of diagnosis. However, the use of contrast agents carries potential risks, and careful consideration is given to their administration, especially in patients with impaired kidney function [61].

The safety of MRI scans has been extensively studied, and they are generally considered to be safe and non-invasive. However, certain precautions must be taken into account. For example, the strong magnetic field generated during an MRI can interfere with metallic objects, such as pacemakers, cochlear implants, or metal fragments in the body. It is crucial to inform the medical staff about any metallic implants or foreign bodies beforehand to ensure patient safety [20].

MRI technology continues to evolve, with ongoing research focused on enhancing image quality, reducing scan times, and developing new imaging sequences. For instance, for cardiac imaging we can enumerate some relatively new sequences such as gated T1 and T2 mapping dedicated to myocardial tissue characterization as well as 3D+t sequences, which capture the heart and large arteries anatomy as well as circulating blood flow velocities in the three space dimensions and throughout the cardiac cycle. One might highlight that main challenges of cardiac imaging and generating such sequences are synchronization to the beating heart as well as the control of the respiratory motion since the heart is located in the middle of our thorax [47].

In conclusion, Magnetic Resonance Imaging (MRI) is a powerful medical imaging technique that utilizes magnetic fields and radio frequency waves to create detailed images of the body's internal structures. It has revolutionized the field of medicine by enabling non-invasive examinations and providing valuable diagnostic information. With ongoing advancements and research in the field of image acquisition and reconstruction as well as image processing, MRIs continue to play a vital role in improving patient care and furthering medical knowledge.

### 1.2.2. MRI Phase Contrast

Phase Contrast (PC) MRI is an advanced imaging technique that provides additional insights into the movement of fluids within the body, including blood flow and muscles movement. While conventional MRI primarily focuses on visualizing anatomical structures, PC-MRI takes advantage of the phase shifts in the MR signal caused by the motion of structures or of flowing fluids [54]. By encoding and measuring these phase shifts, PC-MRI enables the assessment of flow velocities and the visualization of blood flow patterns. In PC-MRI, specialized bipolar gradient waveforms are applied during the MRI scan to sensitively measure the velocity-induced phase shifts. These gradient waveforms are designed to be

sensitive to the direction and speed of fluid flow within the imaging region. The residual phase shifts, after the application of a symmetric bipolar gradient, caused by flowing fluids are then mathematically converted into velocity values using specific formulas. The resulting images, known as velocity maps or phase maps, provide a quantitative representation of the fluid flow velocities [59].

Velocity maps in PC-MRI can be displayed in various ways. One common approach is to overlay the velocity information as a color map onto anatomical images. This color overlay helps visualize the flow direction and speed, with different colors representing different flow velocities. In PC cine imaging, multiple sequential images, often referred to as a cine loop or cine sequence, are acquired over time (often one cardiac cycle) to capture the movement of blood within the cardiovascular system. These cine images are typically displayed as a looped video or series of images, allowing physicians and radiologists to visualize and analyze the blood flow patterns, assess cardiac function, and diagnose various cardiovascular conditions [54].

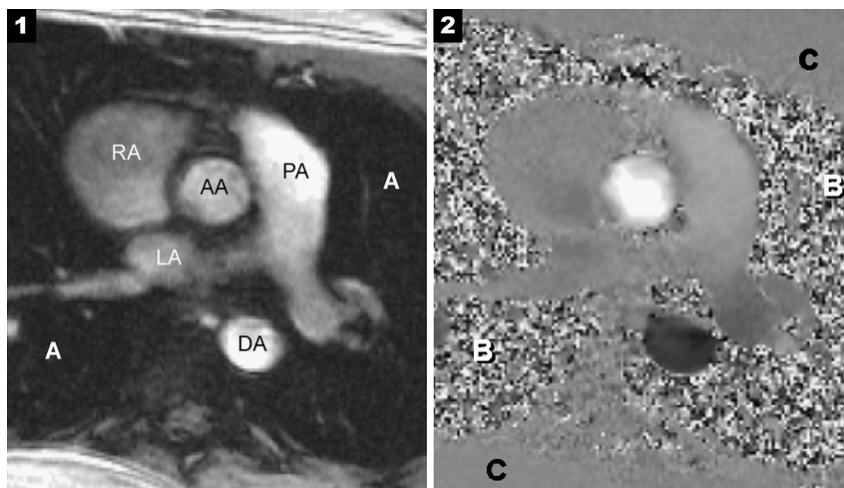


**Figure 1.7:** A phase-contrast velocity mapping scan typically produces two cine images: a magnitude cine image (left) resembling a gradient echo anatomical sequence highlighting white blood, and a grayscale phase cine image (right). In the phase image, upward flow during the systolic phase in the ascending aorta (AA) appears as white-bright contrasts, while downward flow in the descending aorta (DA) is represented as black-dark contrasts. Indistinct noise from the lungs (A) may be visible as random black and white pixels (B), while the chest wall (C) appears uniformly gray as it is stationary [18].

PC-MRI has a wide range of clinical applications. It is particularly valuable in assessing cardiovascular diseases, such as aortic stenosis, congenital heart defects, and valvular disorders such as mitral valve regurgitation. PC-MRI can provide information about blood flow rates,

the presence of abnormal flow patterns (e.g., turbulence or regurgitation), and the assessment of vessel wall shear stress. These quantitative measurements can aid in diagnosing and monitoring cardiovascular conditions, as well as evaluating the effectiveness of treatments or interventions [59].

It is important to note that the implementation and parameters of PC-MRI can vary across different MRI systems and research protocols. The choice of gradient waveforms, imaging parameters, and post-processing techniques can impact the accuracy and quality of the velocity maps obtained. Therefore, it is essential to consider the specific details of each PC-MRI study or clinical application [53, 59].

## 1.3. Medical needs

### 1.3.1. Importance of aortic stiffness measurement

The measurement of aortic stiffness is an important aspect of CVD assessment, providing valuable insights into the health and functioning of the cardiovascular system. Aortic stiffness refers to the loss of elasticity or increased rigidity of the aortic wall, which is the main conduit for blood flow from the heart to the rest of the body.

Aortic stiffness reflects the overall health of the cardiovascular system. It serves as a marker of vascular aging, reflecting the cumulative effects of arterial damage and the presence of systemic diseases such as diabetes, chronic kidney disease, and atherosclerosis [64, 89, 90]. Aortic stiffness can also provide valuable information about the progression of these conditions and the effectiveness of therapeutic interventions.

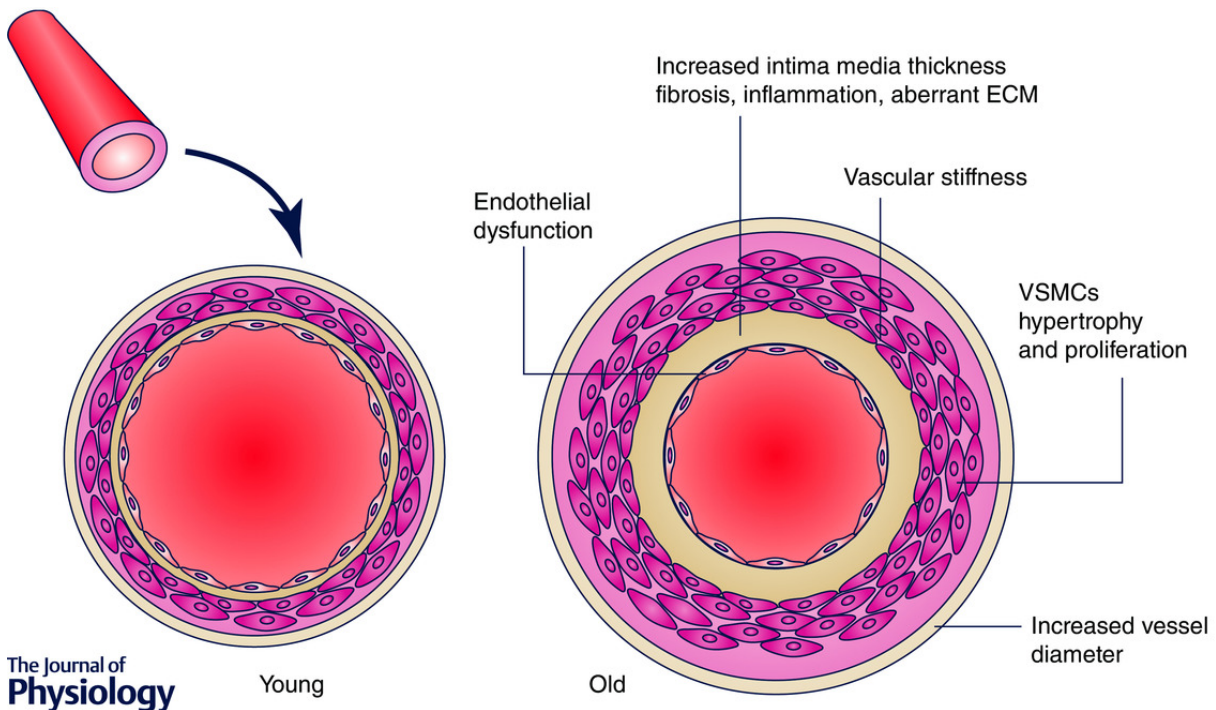


**Figure 1.8:** For a healthy young person (left), the aorta, which is the largest artery in the body, tends to be more elastic. In contrast, as a person ages, the aorta gradually becomes stiffer and loses some of its elasticity. The arterial walls become thicker and less compliant. This age-related arterial stiffness leads to increased resistance to blood flow and impaired ability to accommodate the pulsatile nature of blood pressure changes. Consequently, the pulse wave velocity increases, indicating higher aortic stiffness [21].

A stiff aorta is associated with various adverse cardiovascular events and conditions. First, it is a strong predictor of cardiovascular morbidity and mortality [62]. Increased aortic stiffness contributes to elevated systolic blood pressure and pulse pressure [30], which are known as risk factors in cardiovascular diseases such as primary coronary events and in global cardiovascular mortality [15, 48].

With a stiff aorta, the ability of the arterial walls to expand and contract diminishes. This alteration in arterial compliance leads to changes in the transmission and reflection of the pulse wave. The reflected wave from the periphery encounters a stiffer aorta, resulting in an increased amplitude and earlier return of the wave to the heart during systole [49].

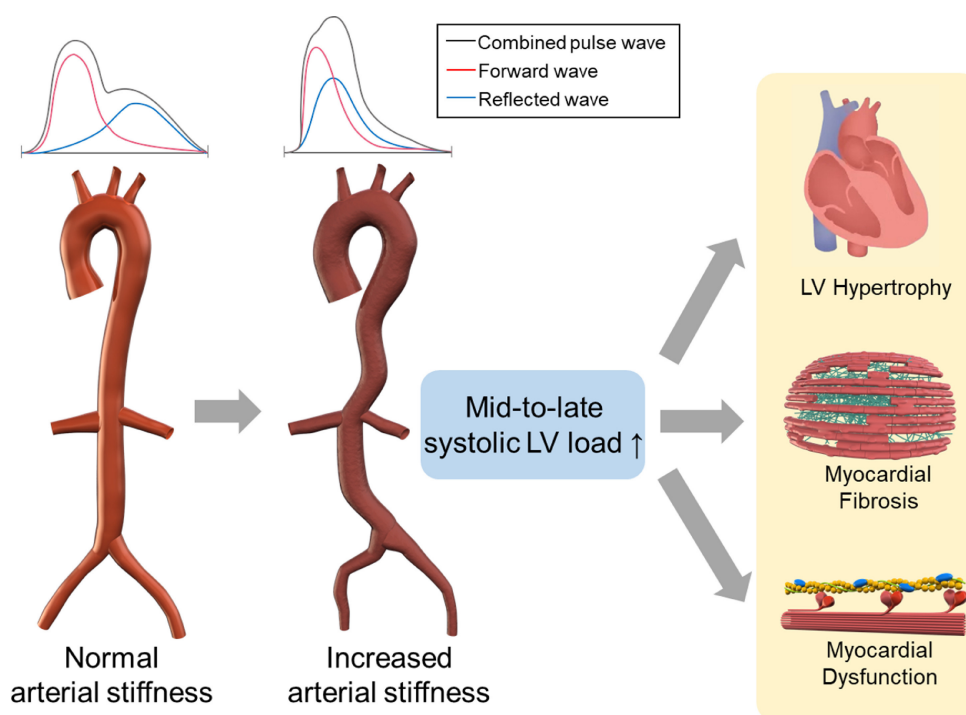


**Figure 1.9:** Representation of the forward and reflected waves in the aorta and the stiffened aorta. The aorta with normal arterial stiffness present two distinct spikes for the forward and reflected waves while for the aorta presenting increased arterial stiffness the two spikes tend to merge into one. This effect leads to CVD described on the right [58].

Moreover, the increased amplitude of the reflected wave can lead to higher systolic blood pressure, known as systolic hypertension, which ultimately lead to adverse left ventricular hypertrophy. It places additional strain on the heart and arterial walls, potentially contributing to further cardiovascular complications [27].

By measuring aortic stiffness, clinicians can assess the impact of various factors on cardiovascular health and make informed decisions regarding patient management. It helps in risk stratification, identifying individuals who may be at higher risk of developing cardiovascular diseases or experiencing cardiovascular events. Additionally, monitoring changes in aortic stiffness over time can provide insights into the efficacy of interventions aimed at improving vascular health, such as lifestyle modifications, pharmacological treatments, and surgical interventions [87].

In summary, the measurement of aortic stiffness is important in the medical context because it provides valuable information about cardiovascular health, risk assessment, and disease progression. It serves as a powerful tool for clinicians to make informed decisions regarding patient management, implement preventive strategies, and monitor

the effectiveness of interventions in improving cardiovascular outcomes.

### 1.3.2. Need of an accurate segmentation

The current tools available for measuring aortic stiffness using MRI images exhibit certain limitations. Many of these tools rely on manual or semi-automated segmentation methods, where the delineation of the aortic lumen is performed by human operators. These manually-supervised approaches, although widely used, presents challenges in terms of subjectivity, variability, and standardization [8, 12]. In the context of cardiovascular studies, the manual annotation of medical images is a time-consuming and laborious task, often resulting in small or sparse annotation sets [8].

The subjectivity inherent to manual segmentation poses a challenge as it can lead to discrepancies in the measurements obtained by different operators, as they often strongly rely on the level of experience of the operator. Variations in contouring techniques, anatomical interpretations, and user expertise can contribute to variability in the final results. The lack of standardized protocols for manual segmentation further exacerbates this issue, making it difficult to achieve consistent and reproducible measurements across studies and clinical settings [12].

To address these limitations, there has been a development of semi-automated methods aiming to expedite lumen area assessment and reduce variability. However, these methods still require significant user interaction and visual quality control, hindering large-scale population-based studies [12].

It is important to acknowledge that the manual and semi-automatic labor involved in segmentation is essential for the creation of a fully automatic solution. The availability of annotated data is crucial for effective training and performance of machine learning algorithms, especially neural networks. Therefore, efforts are being made to develop automated techniques and advanced image analysis algorithms to enhance the efficiency and accuracy of cardiovascular studies [8].

In the assessment of aortic stiffness, PC imaging is widely employed, enabling the estimation of PWV and the evaluation of regional aortic stiffness. To calculate aortic stiffness from MRI data, a precise segmentation of the Ascending Aorta (AAo) and Descending Aorta (DAo) is essential. During the cardiac cycle, the surface of AAo and DAo is extracted from the MRI data, enabling the calculation of their strain. Strain is a measure of how much the vessels deform or stretch during the cardiac cycle. Subsequently, the distensibility of AAo and DAo is calculated by normalizing the strain with the Pulse Pressure, which is the difference between the systolic and diastolic blood pressures. Distensibility represents how

compliant or elastic the vessels are.

To further analyze the flow patterns, velocity images are obtained using PC-MRI. From these velocity images, flow-rate curves are extracted for AAo and DAo over the cardiac cycle. The flow-rate curves provide information about the blood flow in these vessels throughout the heartbeat. By determining the transit time between AAo and DAo from the flow-rate curves and combining it with the distance between AAo and DAo, the aortic arch PWV is calculated. PWV is a crucial parameter for assessing aortic stiffness and vascular health. A more precise segmentation of AAo and DAo ensures accurate calculations of distensibility and PWV, especially when evaluating flow-rate curves.

However, accurate segmentation of the AAo and DAo in PC image sequences can be challenging due to flow-induced intensity variations throughout the cardiac cycle and anatomical complexities. Issues such as flow-induced intensity changes within the lumen, the proximity of the pulmonary artery leading to contour distortion, and the presence of the vena cava affecting the segmentation of the ascending aorta further complicate the process [38].

Therefore, to address these limitations and enhance the efficiency and accuracy of cardiovascular studies, there is a pressing need for the development of automated techniques, advanced image analysis algorithms, and improved segmentation methods.

## 1.4. Aim of the work

The aim of this work is to propose an AI-based method for segmenting dynamic MRIs of the aorta from PC images. The primary goal is to develop a segmentation algorithm using artificial intelligence that can accurately identify and segment the aorta in the dynamic MRI images. Various methods will be explored, employing different hyperparameters, in order to find the most effective approaches. The best-performing methods will be selected and considered for subsequent steps in the research.

Once the segmentation of the aorta is achieved, the next objective is to utilize the segmented images to calculate the velocity of blood flow through the aorta and throughout the cardiac cycle. By comparing the results obtained using the best segmentation methods with the available ground truth data, the researchers aim to accurately quantify the velocity and volumes of blood flow in the aorta.

To assess the performance of the proposed methods, a comparison will be made with the previous software used in the research field, specifically the Laboratoire d'Imagerie Biomédicale (LIB)'s existing software called ARTerial FUNction (ARTFUN). ARTFUN

has been used on more than 7000 patients throughout the world, including our local studies as well as the MESA (multi Ethnic Study of Atherosclerosis) large cohort. The intention is to automate and improve the segmentation process compared to the previous software, validating the advancements made by the AI-based approach.

The last goal is the integration of the developed AI segmentation network into the ARTFUN software to branch our automated segmentation with validated algorithms of PWV and distensibility calculation. This integration aims to enhance the functionality of ARTFUN in terms of aorta segmentation and speed up the processing. By incorporating the AI network, the software is expected to provide more accurate and efficient segmentation results, contributing to improved clinical analysis and diagnosis in the context of aortic dynamics.

Overall, this work focuses on leveraging artificial intelligence techniques to develop a robust and accurate segmentation algorithm for dynamic MRIs of the aorta. By evaluating and comparing the results with existing software, the researchers aim to advance the field and potentially enhance clinical practices related to aorta segmentation and blood flow analysis, by exploring larger populations.

## 2 | Literature Review

This literature review is structured to address three primary areas of interest. Initially, we will provide an overview of the cutting-edge developments in the medical imaging domain. This will offer a holistic view of the prevailing methodologies, technological breakthroughs, and the benchmarks set by leading research.

Subsequently, we'll delve into the world of Deep Learning. Given its revolutionary impact on various disciplines, its influence on medical imaging is undeniable. We'll dissect the Deep Learning methods that align with our study's goals, exploring their potential to revolutionize aortic segmentation processes.

Through this review, we aim to offer readers a clear picture of the current research landscape, setting the foundation for the explorative studies presented later in this thesis.

### 2.1. Medical Imaging

In the realm of medical imaging, modern MRI machines have revolutionized diagnostic capabilities by offering non-invasive and comprehensive insights into the body's internal structures, while studying their geometry, structure, motion and hemodynamics. These sophisticated machines harness the power of strong magnetic fields and precisely tuned radiofrequency pulses, with the strength of the magnet measured in units known as Tesla (T). Among the commonly available options for human imaging are 1.5T, 3T, and 7T machines [60].

Diving deeper into the specifics, research studies by Tanenbaum et al. (2006) underscore the advantages of MRI machines with 3T magnets. They emphasize the increased magnetic field strength of these machines when compared to the 1.5T models. This increase in field strength can lead to better signal-to-noise ratios and improved spatial resolution, both of which can elevate image quality. Notably, 3T MRI machines excel at detailing the subtle complexities of smaller structures like the brain, blood vessels, and joints, solidifying their essential role in medical imaging [80]. The landscape of MRI further unfolds with studies conducted by Triantafyllou et al. (2005) and Runge et al. (2022), where different

magnetic field strengths—ranging from 1.5T, 3T, to 7T—are compared in the context of cardiovascular magnetic resonance (CMR) imaging and the complex realm of 4D flow MRI (velocity encoding images) within the thoracic aorta [73, 81].

Triantafyllou et al. (2005) bring forth a nuanced perspective, revealing the widespread adoption of both 3T and 7T for CMR examinations. Their study paints a landscape where no single field strength emerges as the ultimate choice; instead, each has its unique advantages and challenges. The researchers shine a spotlight on cine imaging that employs retrospectively gated balanced steady-state free precession. This technique proves to be robust across all field strengths, ensuring consistent velocity measurements. However, the study reveals a limitation: lower-SNR acquisitions tend to overestimate peak velocities, while the SNR gains are more modest in the ascending aorta compared to the descending aorta. The reasons for this disparity are attributed to coil sensitivity profile differences and inflow effects [81].

Furthermore, Runge et al. (2022) amplify the discussion around 4D flow MRI in the thoracic aorta, bringing the power of 7T into focus. Their research showcases the feasibility of conducting 4D flow MRI at 7T, unveiling remarkable SNR gains compared to 1.5T and 3T counterparts. However, these gains are not attained without concerted efforts. Successful implementation demands additional sequence modifications, meticulous subject preparation encompassing dynamic B1+ shimming and optimized navigator placements. The study underscores the importance of accelerated acquisition techniques to mitigate contrast agent washout and amplify SNR enhancements [73].

Delving further, Hess et al. (2015) contribute their insights into the assessment of SNR gains in 4D flow studies across different magnetic field strengths and contrast enhancement scenarios. The investigation elucidates subtle discrepancies in signal quality enhancement: it is less pronounced in the ascending aorta compared to the descending aorta. These variations can be attributed to complex factors, among which the coil's sensitivity to signal detection stands out as crucial. Furthermore, the research delves into theoretical simulations indicating that by employing the Ernst angle, there is a potential to modestly augment signal quality at reduced field intensities [39].

Collectively, these studies provide strong evidence. They highlight the advantages of using higher magnetic field strengths, particularly 3T and 7T, for CMR and 4D flow imaging. Enhanced signal-to-noise ratios and image quality emerge as the primary beneficiaries of these advancements. However, the studies also highlight the intricate balance between these technical advances and the challenges that accompany them. Indeed, they mention obstacles like dynamic B1+ shimming and the difficulties related to coil setup that necessitate innovative solutions, along with the optimization of acquisition techniques, while considering

low-flip-angle navigators and faster parallel acceleration methods, which emerges as a pivotal pathway to elevate image quality and mitigate contrast agent washout [39, 73, 81].

As the healthcare landscape evolves, the selection of MRI scanners involves a delicate interplay of financial considerations, operational logistics, the expertise of MRI technologists and the targeted medical application (heart, brain, abdomen, ...). From the ultra-high 7T to the cutting-edge 10.5T systems, each field strength presents its unique benefits and challenges, mirroring the delicate interplay between technological promise and clinical concerns. Whether it's harnessing the unparalleled image resolution of 7T or navigating the technical terrain of 10.5T systems, each choice represents a unique trajectory—a trajectory that converges at the heart of patient care and research optimization. And so, as the MRI community continues to pioneer new frontiers, the landscape remains ever-shifting, promising revelations and discoveries that continue to bridge the gap between the possible and the tangible [50, 82].

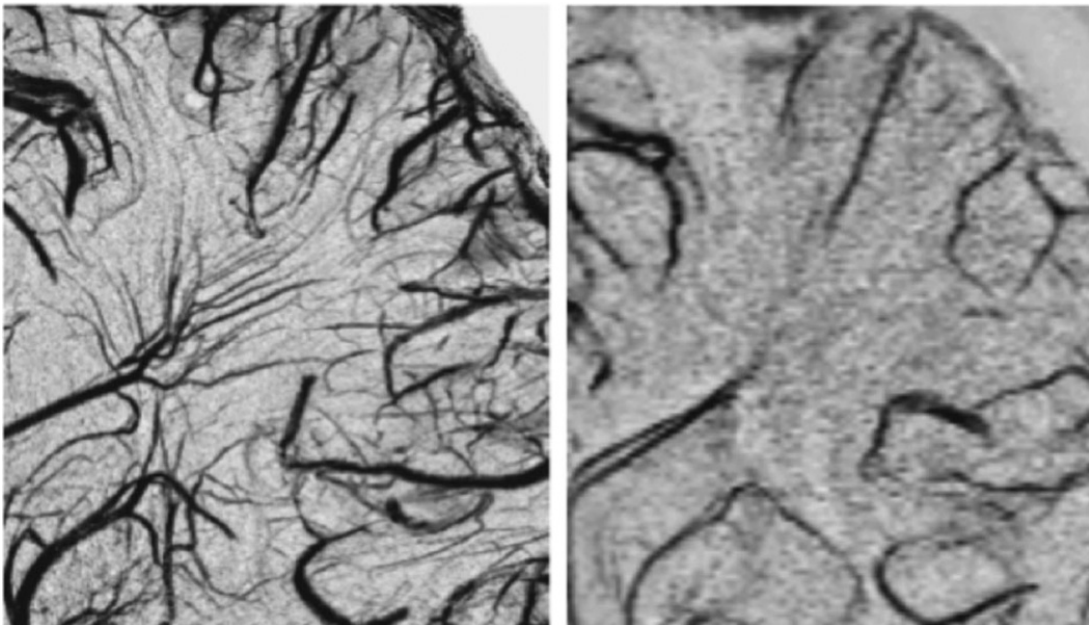


**Figure 2.1:** Here are represented susceptibility weighted imaging at 9.4 T (left) and 3 T (right) in the human brain to depict venous anatomy. The superiority of image resolution offered by the 9.4T machine compared to the 3T is readily apparent [16].

In medical imaging, the particular specifications of MRI machines critically influence the quality and clarity of the images produced. Different machine configurations can yield varied image results, even under similar conditions. Recognizing this, it's essential to consider the discrepancies between MRI machines when evaluating the findings of this thesis. This approach guarantees that the results, Chapter 4, are understood in the right

context, considering any subtleties induced by equipments.

## 2.2. Deep Learning approaches

Deep Learning is a subfield of machine learning that revolves around training artificial neural networks to analyze extensive datasets and generate predictions. By employing interconnected layers of artificial neurons, it excels in deciphering intricate patterns within complex data. Deep Learning has demonstrated significant achievements in various domains, including computer vision, natural language processing, and human-like interaction, revolutionizing the way machines perceive and comprehend information.

### 2.2.1. Convolutional Neural Networks

Before delving into the state-of-the-art of Deep Learning, here is a brief reminder on Convolutional Neural Networks (CNNs). These methods serve as the foundation for the algorithms developed in the literature.

Convolutional Neural Network (CNN) are a specialized type of Deep Learning model designed for processing structured grid-like data, such as images. CNNs have revolutionized the field of computer vision and achieved remarkable success in tasks like image classification, object detection, and image segmentation.

At the core of a CNN are convolutional layers. These layers are responsible for learning and extracting meaningful features from the input data. Each convolutional layer consists of a set of learnable filters or kernels. These filters are small matrices that are convolved (slid) across the input image in a systematic manner. By applying the convolution operation, the filters detect different visual patterns or features, such as edges, textures, or shapes. The result is a set of feature maps that represent the activation of each filter at different spatial locations [51].

Stride and padding are parameters that control the behavior of the convolution operation. Stride determines the step size at which the filter is moved across the input. A larger stride value reduces the spatial dimensions of the output feature maps, whereas a stride of 1 preserves the spatial size. Padding involves adding additional border pixels to the input image to maintain spatial dimensions and prevent information loss during convolutional operations [46].

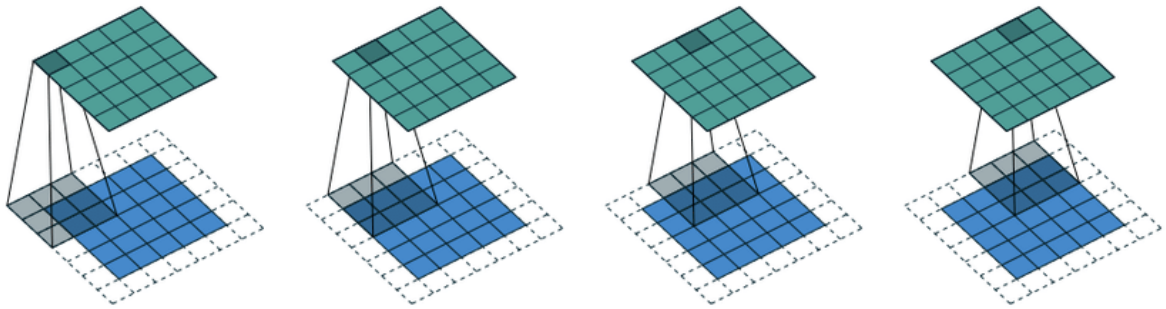
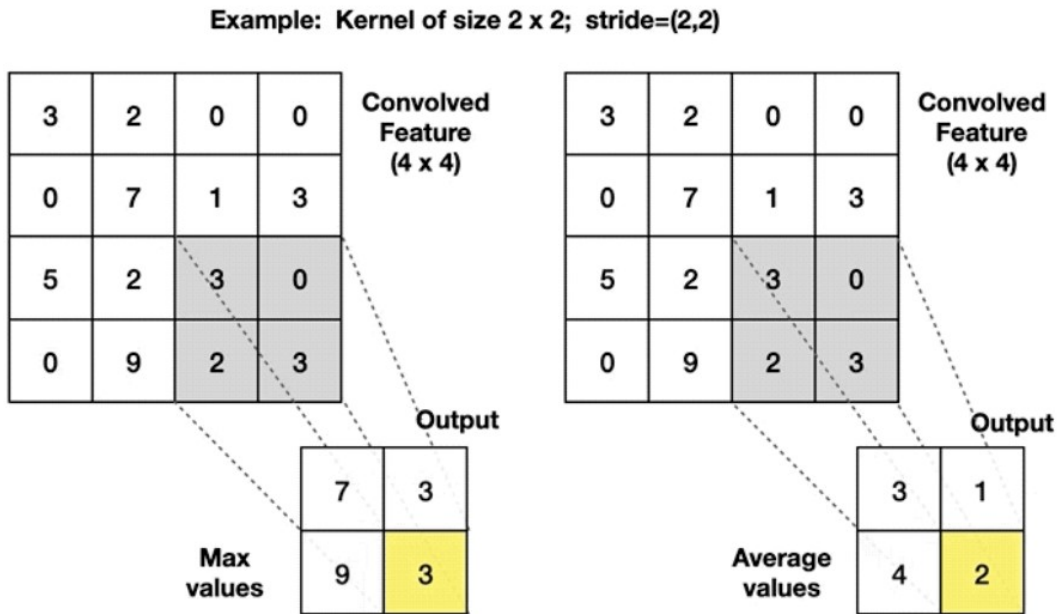


Figure 2.2: Example of convolution steps with a padding of one, stride of one and a filter size of  $3 \times 3$  [14].

To make the learned features more robust and invariant to small variations in the input, CNNs often include additional layers such as activation functions and pooling layers. Activation functions introduce non-linearity into the network, allowing it to learn complex relationships between features. Common activation functions used in CNNs include Rectified Linear Unit (ReLU), sigmoid, and tanh [51].

Pooling layers, such as max pooling or average pooling, are used to downsample the spatial dimensions of the feature maps. Pooling helps reducing the computational complexity of the network and makes it more robust to variations in the input by summarizing the presence of features in a local neighborhood. By discarding some spatial information, pooling also contributes to a degree of translation and rotation invariance, meaning the network can recognize patterns regardless of their exact position in the input [67].



**Figure 2.3:** On the left, the Max Pooling takes the highest value of the area covered by the kernel. On the right, the Average Pooling computes the average value from the covered area [67].

Typically, a CNN consists of multiple stacked convolutional layers, interspersed with activation and pooling layers. Towards the end of the network, fully connected layers are often added to perform the final classification or regression task. These fully connected layers take the high-level features extracted by the earlier layers and map them to the desired output. The network is trained end-to-end using labeled data, where the parameters of all the layers are optimized through a process called backpropagation, minimizing a suitable loss function [46].

Training a CNN involves several important aspects, including loss functions and optimization algorithms, backpropagation and gradient descent, batch training, learning rate scheduling, and evaluation metrics for classification tasks.

Loss functions quantify the discrepancy between the predicted outputs of a CNN and the true labels in the training data. For classification tasks, commonly used loss functions include cross-entropy loss, which measures the dissimilarity between predicted probabilities and groundtruth labels [33].

Optimization algorithms determine how the network learns and updates its parameters during training. Gradient descent is a widely used optimization algorithm that utilizes the gradients of the loss function with respect to the network parameters to iteratively update the

weights. Popular variations of gradient descent include stochastic gradient descent (SGD) and adaptive algorithms like Adam, which adjust the learning rate based on the history of gradients [44].

Batch training involves dividing the training data into smaller subsets called batches. Instead of updating the weights after each individual sample, the network updates the weights based on the average gradient computed over the batch. This approach improves computational efficiency and stabilizes the training process [33].

Evaluation metrics and loss functions are pivotal for assessing the performance of a trained CNN on classification and segmentation tasks. Common metrics include accuracy, which measures the proportion of correctly classified samples, as well as precision, recall, and F1-score, which provide insights into the trade-off between correctly identifying positive samples and minimizing false positives or false negatives [33]. In the context of medical image segmentation, many loss functions exist, such as distribution-based and region-based losses, which are variants of cross entropy and Dice loss respectively. There are also boundary-based losses, which minimize the distance between two boundaries but show some similarities to Dice loss, since both employ region-based methods. Interestingly, compound loss functions, which combine different types of loss functions, often emerge as superior choices for medical image segmentation tasks, particularly for handling imbalances [52].

Advanced CNN architectures have significantly advanced the field of Deep Learning, with two notable examples being VGG16 and ResNet50. VGG16, introduced by Simonyan and Zisserman in 2014, is renowned for its simplicity and effectiveness. Comprising 16 layers, including multiple convolutional and pooling layers, followed by fully connected layers, VGG16 utilizes small  $3 \times 3$  convolutional filters stacked together to enable deeper representations. This architecture excels at learning and representing complex patterns in images, rendering it well-suited for various computer vision tasks [78]. On the other hand, ResNet50, proposed by He et al. in 2015, introduced the concept of residual connections. Addressing the vanishing gradient problem in deep networks, this architecture allows information to flow directly through shortcut connections. Stacking residual blocks, ResNet50 efficiently trains extremely deep networks while maintaining performance and accuracy. The introduction of residual connections has profoundly impacted the successful training of very deep CNNs [37].

Transfer learning is a technique that capitalizes on pre-trained CNN models for new tasks or datasets. Instead of training a CNN from scratch, transfer learning leverages knowledge and features learned from large-scale datasets. By fine-tuning pre-trained models on new datasets, transfer learning achieves faster convergence and often outperforms training from

scratch, especially when the new dataset is small or similar to the original dataset used for pre-training [88].

Various frameworks are available for developing Deep Learning methods, among them, TensorFlow stands out as a widely adopted open-source Deep Learning framework developed by Google. It provides a comprehensive ecosystem for building, training, and deploying machine learning models. TensorFlow offers a flexible and scalable platform that supports both low-level operations and high-level abstractions, allowing users to define and train complex neural networks. Its graph-based execution model and extensive library of pre-built functions make it suitable for a wide range of applications [2, 5]. PyTorch is another popular open-source Deep Learning framework that emphasizes flexibility and dynamic computational graphs. Developed by Facebook's AI Research lab, PyTorch enables intuitive models development and efficient debugging through its imperative and Pythonic programming interface. It provides automatic differentiation, enabling easy implementation of custom architectures and dynamic adjustments during training. PyTorch's popularity has grown rapidly due to its user-friendly design and strong support from the research community [1, 65].

When deploying CNNs, there are crucial factors to consider, namely ethical considerations and privacy protection. As CNNs may process sensitive or personal data, concerns arise regarding data privacy and security. Protecting privacy involves implementing techniques such as data anonymization, secure storage practices, and responsible data handling policies. Respecting individuals' privacy rights and adhering to data protection regulations are fundamental principles for the ethical deployment of CNNs [9, 69]. These considerations become even more important in the context of medical data.

Biases can be unintentionally introduced into CNNs due to biased training data or inadequate representation of diverse demographics. This can result in unfair or discriminatory outcomes. Addressing biases in CNNs requires careful consideration of dataset biases, ensuring balanced and representative training data, and implementing fairness-aware evaluation metrics [17].

CNNs have certain limitations and challenges that impact their applicability and effectiveness:

- **Interpretability:** CNNs are often seen as black boxes, making it difficult to interpret and understand their decision-making process. Enhancing the interpretability of CNNs is an ongoing research area [74].
- **Computational Requirements:** Training and inference in CNNs can be computationally

demanding, requiring powerful hardware and substantial computational resources. Optimizing CNN architectures and leveraging specialized hardware can help address these challenges [45].

CNNs have demonstrated exceptional performance in various computer vision tasks and have become a cornerstone of modern artificial intelligence systems. With their ability to automatically learn and extract hierarchical features from images, CNNs have greatly advanced the field of image understanding and paved the way for applications in areas like autonomous vehicles, medical imaging, and video analysis. Nevertheless, despite their successes, CNNs do encounter certain limitations. Thus, our exploration will focus on studying new methods that transcend simple CNN architectures.

### 2.2.2. UNet

The UNet architecture is a CNN architecture that was specifically designed for semantic segmentation tasks, where the goal is to classify each pixel in an image into specific classes or categories. It was proposed by Olaf Ronneberger, Philipp Fischer, and Thomas Brox in 2015 and has since then become a widely used model for various medical imaging applications [72, 77].

The UNet architecture gets its name from its U-shaped design. It consists of an encoder path and a decoder path, which are connected by a bottleneck layer. The encoder path, similar to a traditional CNN, gradually reduces the spatial dimensions of the input image while extracting higher-level features. This is achieved through a series of convolutional and pooling layers. The pooling layers downsample the feature maps to capture increasingly abstract representations [19, 72].

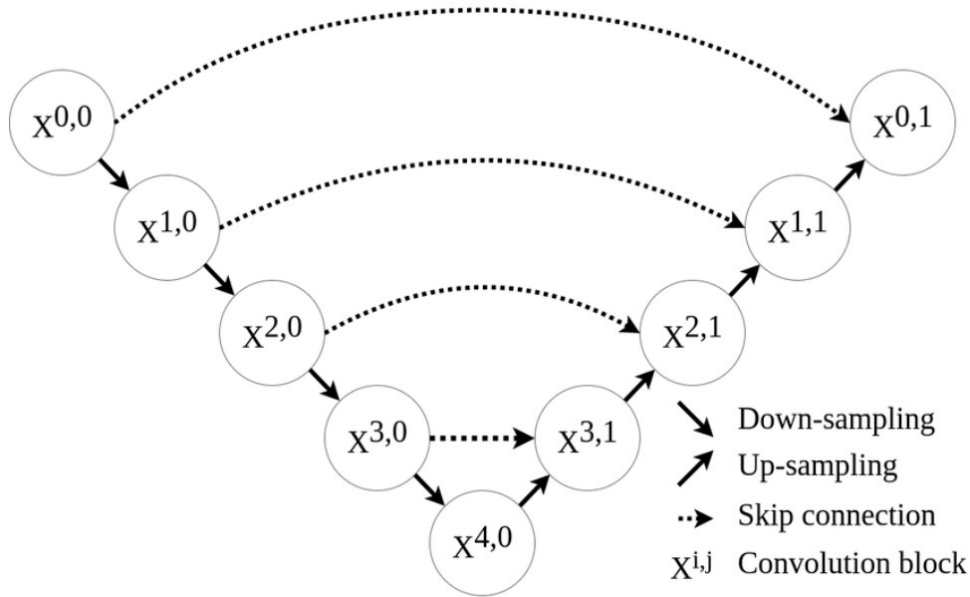


Figure 2.4: A representation of the UNet architecture, the encoder path is represented by the Convolution blocks  $X^{0,0}$  to  $X^{3,0}$ . The bottleneck is represented by the Convolution block  $X^{4,0}$  and the decoder path is represented by the Convolution blocks  $X^{3,1}$  to  $X^{0,1}$  [93].

The decoder path, aims to recover the spatial information and generate a dense segmentation map. It consists of a series of upconvolutional (also known as transpose convolutional) layers, which gradually increase the spatial resolution of the feature maps. The upconvolutional layers are followed by concatenation with the corresponding feature maps from the encoder path, which allows the decoder to leverage both local and global information. This skip-connection mechanism helps to preserve fine-grained details during the upsampling process [19, 72].

The bottleneck layer acts as a bridge between the encoder and decoder paths, providing a concise representation of the input image's features. It allows the decoder to access both low-level and high-level features, facilitating accurate segmentation. The skip-connections, combined with the symmetric U-shape design, enable the UNet architecture to capture both contextual information and spatial details, making it effective for tasks such as medical image segmentation [19, 72].

The UNet architecture is typically trained using labeled training data, where the network is optimized to minimize a suitable loss function, such as cross-entropy loss or dice loss. During training, the network learns to predict pixel-wise class probabilities, allowing it to generate segmentation maps for unseen images [72].

The UNet architecture has proven to be highly effective in various medical and

histological image analysis tasks, such as organ segmentation, tumor detection, and cell segmentation. Its ability to leverage both local and global information, combined with the skip-connection mechanism, enables accurate and detailed segmentation even with limited labeled data [77, 92].

The U-Net architecture, while pioneering in the domain of biomedical image segmentation, it may exhibit some constraints. Firstly, its design is parameter-intensive, increasing computational demands and often requiring robust hardware for optimal performance. Secondly, its efficacy is deeply rooted in the presence of high-quality annotated data. This makes it less adaptable in situations where datasets are limited or inherently imbalanced. Lastly, its ability to generalize presents challenges. Though U-Net might perform exceptionally on the tasks it's specifically trained for, it can fail when presented with images that deviate from its training context, unless adequate fine-tuning is undertaken [93].

UNet++ is an advanced variation of the UNet architecture, designed to address the limitations of the original UNet and further enhance semantic segmentation performance. Introduced as an evolution of the UNet, UNet++ incorporates a nested architecture that significantly improves the model's ability to capture multi-scale context and produce accurate segmentation masks [77].

The key innovation of UNet++ lies in its encoder and decoder paths. In the encoder path, instead of using a single UNet block at each level, UNet++ incorporates multiple nested UNet blocks. Each nested UNet block captures features at different scales, allowing the model to gather rich contextual information. This multi-scale representation enables UNet++ to handle objects of varying sizes and better understand the overall context of the scene [77, 93].

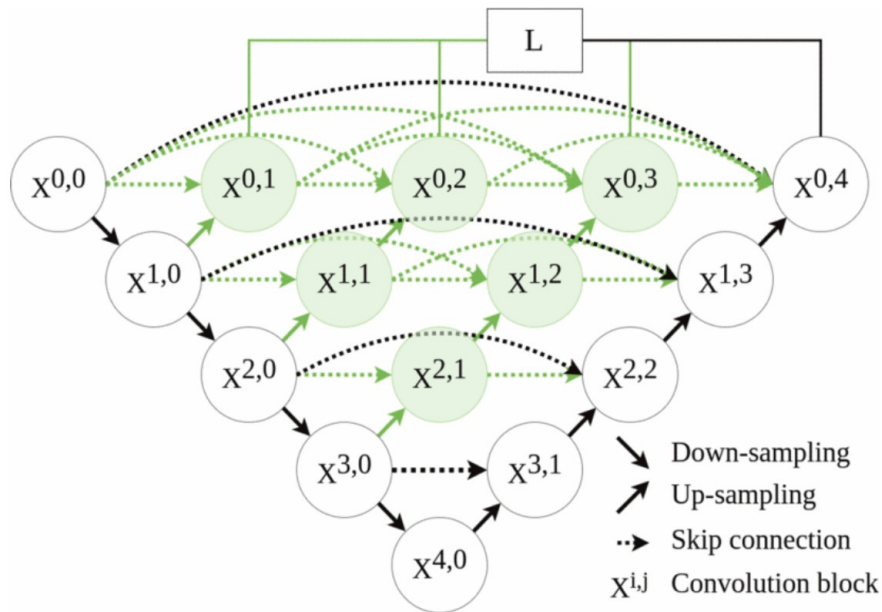


Figure 2.5: Presentation of the of the UNet++ structure. The backbone of the method corresponding to the UNet is represented in black and the new blocks and skip connections are represented in green, highlighting the fact that the previous skip-connection area has been densified [93].

As information flows through the decoder path of UNet++, the multi-scale skip connections play a vital role. Unlike the original UNet, which uses only one skip connection per level, UNet++ introduces multiple skip connections at each level, forming a hierarchy of skip connections between the corresponding UNet blocks in the encoder and decoder. These skip connections enable the decoder to receive multi-scale features from the encoder, effectively combining fine-grained details and high-level context. Consequently, the model gains the ability to localize object boundaries more accurately and produce more refined segmentation masks [91].

One of the main advantages of UNet++ is its improved accuracy, particularly when dealing with objects of different sizes. The nested architecture and multi-scale skip connections allow the model to capture both local and global context, making it robust to scale variations. As a result, UNet++ excels in scenarios where the sizes and shapes of objects vary significantly within the same image. In medical imaging, UNet++ has been widely adopted for segmenting various anatomical structures, tumors, and lesions [77].

In conclusion, UNet++ represents a significant advancement in semantic segmentation architecture. With its nested UNet blocks and multi-scale skip connections, it achieves

state-of-the-art performance, providing precise and robust segmentation results. This novel approach has opened up new possibilities in computer vision and as research progresses, UNet++ is likely to remain a prominent choice for various segmentation challenges, contributing to the development of more accurate and efficient models in the future [91, 93].

### 2.2.3. Recurrent Neural Networks

Given that our images are dynamic 2D series (2D+t), it is important to explore the state-of-the-art in terms of time-dependent Deep Learning methods. These methods focus on capturing temporal dependencies and variations in sequential data, allowing us to leverage the time dimension to enhance the understanding and analysis of dynamic imaging [31].

Recurrent Neural Networks (RNN) are a type of neural network that can process sequential data by introducing the concept of recurrent connections. Unlike feedforward neural networks, which process input data independently, RNNs have connections that allow information to persist and flow across different time steps. This makes them suitable for tasks that involve sequential or time-series data, such as natural language processing and speech recognition [42].

At the core of an RNN is the recurrent connection, which enables the network to maintain an internal memory or hidden state that captures information about the past inputs. This hidden state is updated at each time step, combining the current input with the previous hidden state. The key idea behind RNNs is that the hidden state serves as a way to recall and incorporate information from previous steps into the current computation [41].

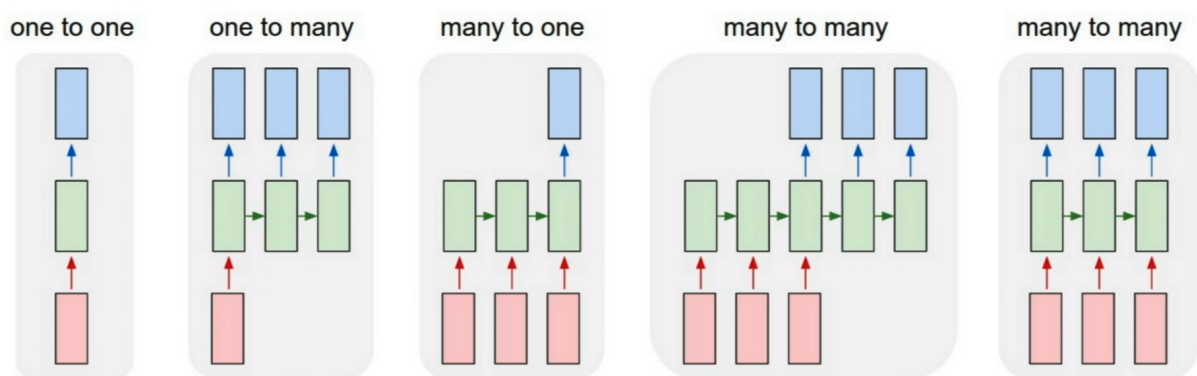


**Figure 2.6:** RNNs offer a flexible framework for sequence processing, accommodating varied configurations. They can handle simple 'one-to-one' interactions, expand to 'one-to-many' or 'many-to-one' for tasks like image captioning or sentiment analysis, and even operate in a 'many-to-many' mode for applications like machine translation. This adaptability underscores RNNs' broad utility in diverse domains [42].

However, traditional RNNs suffer from the "vanishing gradient" problem, where the gradients used to update the weights during training can diminish over time, making it challenging for the network to capture long-term dependencies. To address this issue, the Long Short-Term Memory (LSTM) architecture was introduced [10].

LSTMs are a type of RNN that are designed to better capture long-term dependencies by incorporating memory cells. Each LSTM cell contains three main components: an input gate, a forget gate, and an output gate. These gates regulate the flow of information within the cell, allowing it to selectively remember or forget information [40].

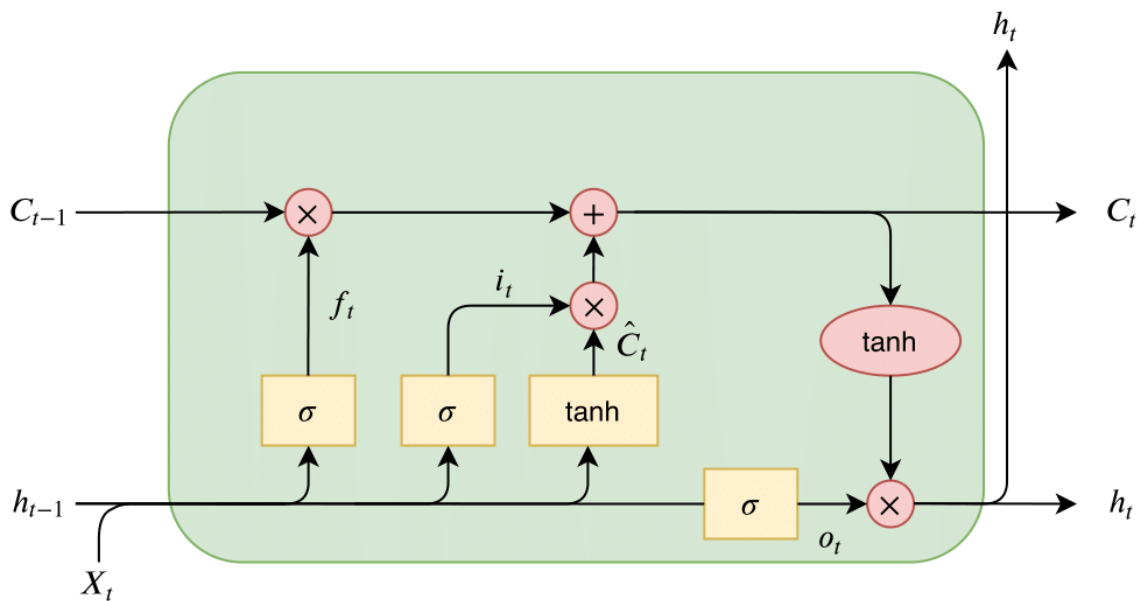


Figure 2.7: The LSTM cell architecture comprises key components like  $X_t$  for the input time step,  $h_t$  as the output, and  $C_t$  representing the cell state. Integral gates such as  $f_t$  (forget gate),  $i_t$  (input gate),  $o_t$  (output gate), and  $\hat{C}_t$  (internal cell state) play pivotal roles in its functionality. Notably, operations enclosed within the light red circle are executed pointwise [41].

The input gate determines how much new information should be added to the cell's memory. It takes into account the current input and the previous hidden state and applies a sigmoid function to produce values between 0 and 1, indicating the amount of information to retain [10, 41].

The forget gate decides which information from the previous memory cell should be discarded. It takes the current input and the previous hidden state as input and uses a sigmoid function to produce forget coefficients between 0 and 1. These coefficients determine the degree to which each element of the previous memory cell is forgotten [10].

The output gate controls how much information from the current memory cell is exposed to the rest of the network. It combines the current input and the previous hidden state, applies a sigmoid function, and produces an output between 0 and 1. This output is multiplied by the cell's memory state to generate the current hidden state and output [10, 41].

By using these gates, LSTM cells can selectively retain or discard information over time, making them well-suited for tasks that require modeling long-term dependencies. The ability to preserve information over several time steps and mitigate the vanishing gradient problem has made LSTMs widely used in various applications, including machine translation, sentiment analysis, and speech recognition [40].

During training, the parameters of the LSTM network are optimized using backpropagation through time, which is an extension of backpropagation for sequential data. The gradients are computed and propagated through the time steps, allowing the network to learn the optimal weights for capturing sequential patterns [33, 34].

LSTM networks, while groundbreaking in their capacity to retain long-term dependencies in sequences, have certain limitations. One primary constraint is their unidirectional nature, which means they process sequences from the start to the end, potentially missing out on context that can be gleaned from future states in the sequence [76].

Bidirectional Long Short-Term Memory (BiLSTM) is an extension of the LSTM model, a type of RNN). While LSTM processes sequences of data in a forward direction, BiLSTM adds a bidirectional aspect to the model, allowing it to analyze sequences both in the forward and backward directions simultaneously [76].

The key idea behind BiLSTM is to capture not only the past context but also the future context of each element in the input sequence. By processing the input sequence in both directions, BiLSTM can effectively gather information from the entire context, which can be especially useful in tasks where the output depends on the complete sequence, such as natural language processing, speech recognition, and sentiment analysis [43].

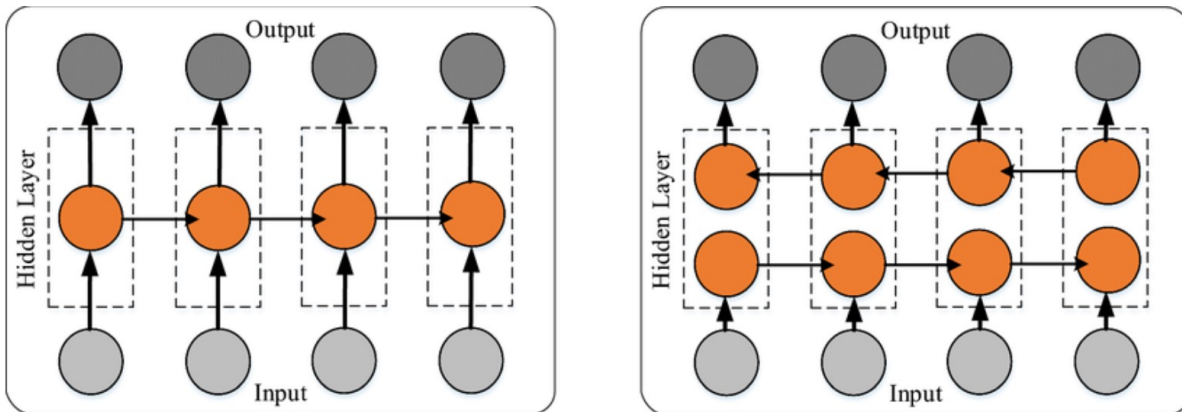


Figure 2.8: On the left, LSTM, on the right, BiLSTM [75].

In BiLSTM, the input sequence is duplicated, and two separate LSTM layers are used: one for processing the original sequence forward, and the other for processing the reversed sequence. The outputs of both LSTM layers are then combined to create the final output of the BiLSTM model [43].

By considering both past and future information, BiLSTM can better handle long-range dependencies and make more informed predictions. This makes it a powerful tool for tasks that involve sequential data with complex patterns and dependencies. BiLSTM has found widespread applications in various fields, showcasing its effectiveness in capturing bidirectional context and achieving improved performance in a range of sequence modeling tasks [75, 76].

#### 2.2.4. Complex methods based on Deep Learning

Deep Learning has paved the way for groundbreaking innovations in various domains, especially in image analysis. Building upon this foundational knowledge, several researchers have ventured into developing more specialized and nuanced methods. Among these, three papers stand out for their inventive approaches. The work by Biasioli et al. delves into cardiovascular imaging by segmenting regions of interest through the Circular Hough Transform and further refining these regions using the Random Forest algorithm. In contrast, Bai et al. harness the capabilities of RNN with the UNet algorithms, creating a harmonized method for sequential image analysis. Lastly, Hann et al. methodology combines a diverse ensemble of six UNets, optimizing segmentation results based on the Dice Similarity Coefficient. Each of these papers, while rooted in Deep Learning principles, presents a unique lens through which image analysis can be approached, enhancing the intricate landscape of research in this field.

### Biasioli et al. method

The Biasioli et al. method presents an innovative approach for segmenting ROI in cardiovascular imaging. The process begins with the extraction of the ROI through the Circular Hough Transform, which efficiently identifies the anatomical boundaries of the Ascending (AAo) and Descending (Dao) Aorta from the surrounding image data [12]

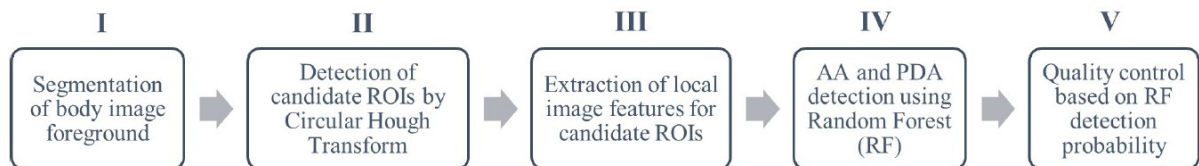


Figure 2.9: Illustration of an algorithm flowchart, outlining the process for automated detection and localization of the AAo and DAAo. The flowchart also highlights the integral steps for quality control, ensuring accuracy and precision in the algorithm's execution.

Once the ROI is cropped, the method focuses on segmenting the AAo and DAAo using a Random Forest algorithm. Random Forest (RF) is a powerful machine learning technique known for its ability to handle complex and high-dimensional data, making it well-suited for accurate segmentation tasks. By training the RF model on annotated data, the method can effectively classify and delineate the AAo and DAAo regions with high precision [12].

The combination of Circular Hough Transform for ROI extraction and the application of RF for AAo and DAAo segmentation enabled Biasioli et al. to achieve robust and reliable results in cardiovascular imaging. This method contributes to the advancement of medical image analysis by providing a practical and automated solution for precisely identifying and delineating key regions of interest in cardiovascular MRI images [12].

### Bai et al. method

The Bai et al. method introduces a novel approach for aortic image analysis, leveraging the power of RNN and UNet algorithms. The core of their method involves the integration of these two techniques to enhance the understanding and processing of sequential image data [8].

In this method, a sequence of images serves as the input to the BiLSTM. Before being fed into the BiLSTM, each individual image undergoes processing through a UNet algorithm. By passing the images through the UNet algorithm first, the Bai et al. method aims to enrich the features and representations of each frame before temporal analysis [8].

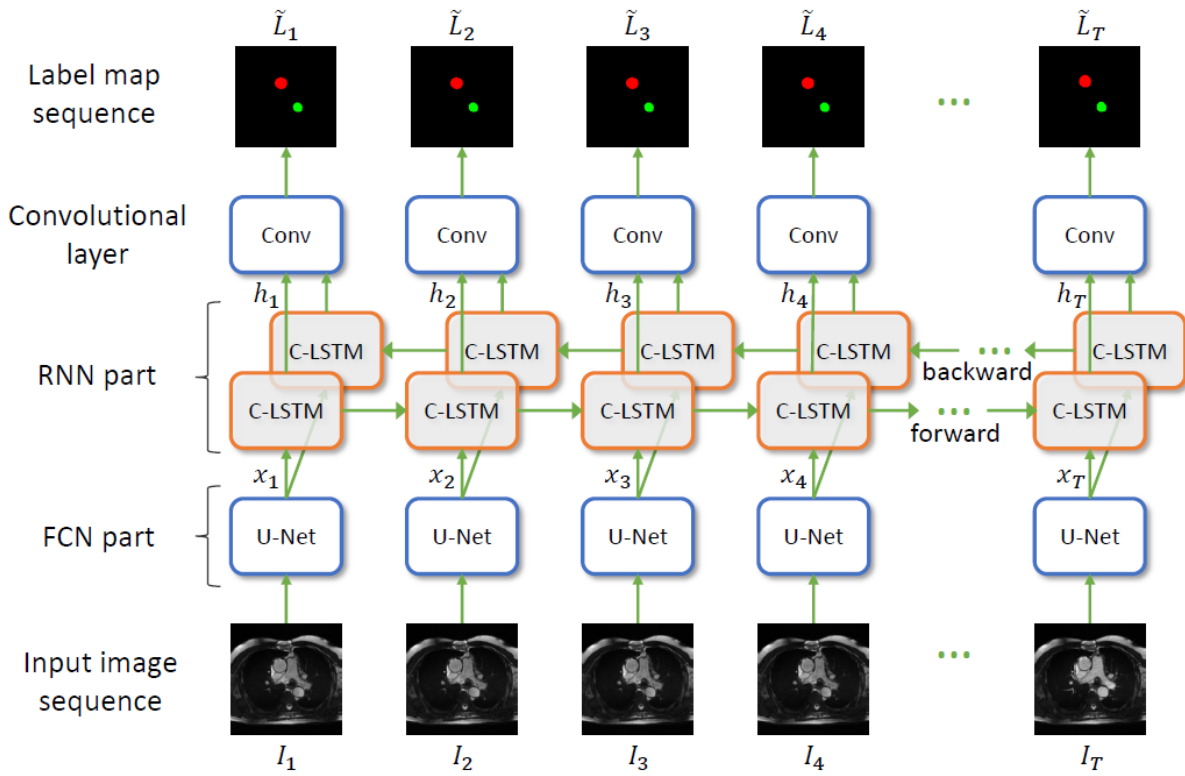


**Figure 2.10:** The diagram illustrates the method's architecture. Initially, an input image sequence is processed by a UNet. The output from the UNet is then channeled into a BiLSTM. Following this, the sequential output passes through a convolutional layer, culminating in the retrieval of the Label Map Sequence.

The BiLSTM, known for its capacity to handle sequential data, processes the pre-processed image sequence. The BiLSTM's recurrent connections allow it to capture temporal dependencies and patterns across frames, effectively modeling the dynamic evolution of the image sequence [8].

By combining the UNet's powerful image feature extraction capabilities with the temporal analysis of BiLSTMs, the Bai et al. method demonstrates significant advancements in understanding and interpreting sequential image series. This innovative fusion of techniques opens up new possibilities for various applications, including video analysis, action recognition, and dynamic medical imaging, where capturing temporal context is crucial for accurate data analysis. Bai et al.'s method contributes to the growing field of Deep Learning, enhancing the capabilities of image analysis in both research and practical domains [8].

## Hann et al. method

Hann et al. method introduces an intricate segmentation process, harnessing the power of six distinct UNets. These UNets are not just diverse in number but also differentiated by their individual architectural depths and the number of skip connections they had. Such variation is designed to cater to different image intricacies and to optimize the segmentation output for a wide range of scenarios. After the application of these UNets, an inter-segmentation Dice Similarity Coefficient (DSC) is meticulously calculated, offering a quantitative measure of the overlap between the segmentations. With these results in hand, two distinct pathways open up for consideration. Practitioners can either employ the automatic quality scoring system to craft a novel, optimized segmentation by combining the strengths of the different UNets. Alternatively, if a singular, standout result is desired, the quality control-guided approach can be employed to select one standout segmentation from the six, based solely on the highest DSC score [35].

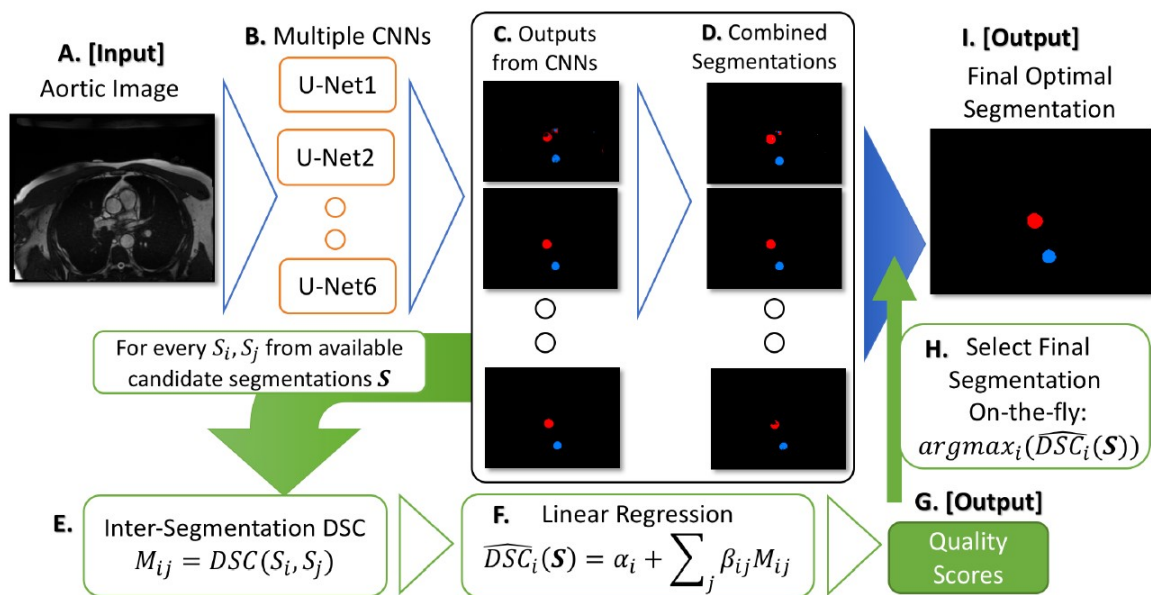


Figure 2.11: Hann et al.'s method initiates with an input (A), deploying six varied UNets or CNNs (B). These produce distinct outputs (C) which merge into combined segmentations (D). An inter-segmentation DSC (E) assesses the overlap. Post this, a linear regression (F) produces quality scores (G). Practitioners can then opt for a unified result or select based on the highest DSC (H), culminating in the final output (I).

Upon gauging the DSC values, two alternatives can be considered: one involves an automatic quality scoring system that crafts a new segmentation steered by the DSC evaluations. This mechanism extracts the finest segmentations from the UNet collection

[35].

On the other hand, the quality control-oriented segmentation technique picks a single segmentation from the six UNet results, placing emphasis on the one with the optimal DSC value. This tactic approach is dedicated to bolstering the precision and trustworthiness of the concluding segmentation [35].

In summation, Hann and team meld the strengths of several UNet designs and capitalize on the DSC to refine the segmentation task, resulting in accurate outcomes. Their methodology offers the latitude to either autonomously sculpt a new segmentation or zero in on the premier from the collection, unlocking profound implications especially in arenas like medical imaging and computer vision [35].

Deep Learning has revolutionized image analysis, and our project is set to benefit from the techniques highlighted in the mentioned studies. We will be drawing from Biasioli et al.'s methods in cardiovascular imaging, Bai et al.'s combination of RNN and UNet, and Hann et al.'s ensemble of UNets. By integrating these innovative approaches, our aim is to advance image analysis, building on the strong groundwork these researchers have laid down.

# 3 | Materials and Methods

This chapter provides a detailed exploration of the research framework from various angles. In Section 3.1, we introduce the dataset employed for our study, offering insights into its origin, composition, and relevance. Section 3.2 is dedicated to elucidating the meticulous data preprocessing steps undertaken to ensure the cleanliness and reliability of our dataset. The subsequent Section 3.4 highlights the metrics used to assess our models' performance and effectiveness. Finally, in Section 3.3, we delve into the deep learning models utilized in our analysis, offering a clear explanation of their structures, parameters, and functions.

## 3.1. Dataset

This study is centered on the utilization of 2D dynamic MRI images of the human aorta. Also known as cine MRI or cardiac MRI, 2D dynamic MRIs are a type of medical imaging technique that captures a series of images of a moving organ, usually the heart, as it moves over time. The "2D" refers to the fact that these images are slices taken from a specific plane within the body. The "dynamic" aspect refers to the ability to capture these images in rapid succession, creating a sequence that shows how the organ changes its shape and moves during various phases of a cardiac cycle (heartbeat) [28].

During a cardiac MRI scan, a series of images is acquired over multiple heartbeats. This allows medical professionals to study how the heart's chambers contract and relax, how blood flows through the heart's different chambers and vessels, and how various structures of the heart move synchronously or asynchronously [25].

This study was conducted during an internship at the LIB, which has strong collaborations with two of the biggest hospitals in Paris, namely La Pitié Salpêtrière Hospital and the European Hospital Georges Pompidou, facilitating access to medical data for algorithmic training. The data used in this study was sourced from these collaborations.

The dynamic 2D MRIs considered in this study are obtained from an axial view of the heart. These images are particularly valuable for diagnosing heart conditions, evaluating heart function, and assessing issues like the pumping efficiency of the heart, the presence of any

abnormalities in the heart's structure, and the effects of heart diseases on such characteristics. The ability to see the beating heart in motion provides insights that static images cannot offer, making 2D dynamic MRIs an essential tool in clinical routine medical imaging [83].

To streamline the management and analysis of these images, a standardized format known as DICOM is employed. DICOM stands for "Digital Imaging and Communications in Medicine." It is a standard format used in the field of medical imaging to store, transmit, and exchange various types of medical images and related information (Figure 3.1). DICOM serves as a common language that enables different medical devices and systems to communicate effectively and share medical images [7].

```

Dataset.file_meta -----
(0002, 0000) File Meta Information Group Length  UL:
(0002, 0001) File Meta Information Version      OB:
(0002, 0002) Media Storage SOP Class UID       UI:
(0002, 0003) Media Storage SOP Instance UID    UI:
(0002, 0010) Transfer Syntax UID               UI:
(0002, 0012) Implementation Class UID         UI:
(0002, 0013) Implementation Version Name      SH:
(0002, 0016) Source Application Entity Title   AE:
(0002, 1016)                                  AE:
-----
(0008, 0005) Specific Character Set            CS:
(0008, 0008) Image Type                       CS:
(0008, 0012) Instance Creation Date           DA:
(0008, 0013) Instance Creation Time          TM:
(0008, 0016) SOP Class UID                    UI:
(0008, 0018) SOP Instance UID                 UI:
(0008, 0020) Study Date                       DA:
(0008, 0021) Series Date                      DA:
(0008, 0022) Acquisition Date                 DA:
(0008, 0023) Content Date                     DA:

```

**Figure 3.1:** The image showcases an example of DICOM metadata. On the left, reference standardized numbers are displayed alongside the corresponding variable names. To the right, the corresponding values have been purposely removed for privacy concerns.

The DICOM standard ensures interoperability among various imaging devices, such as MRI, Computed Tomography (CT) and ultrasound scanners and devices. It allows images from different manufacturers, systems and acquisition centers to be viewed and analyzed on a common platform [7].

This work focuses specifically on MRI velocity encoding or phase contrast images acquired for the evaluation of aortic geometry and flow. Accordingly, within each DICOM file, there are two key components: modulus images that contrast and distinct structures of the

aorta, and velocity images (with a through plane encoding of the velocity) that illustrate the varying velocities of these structures (flowing blood essentially in the arteries) in a pixel-wise fashion. In our methodology, the modulus images play a central role by enabling accurate segmentation of both the Ascending and Descending Aorta (AAo and DAo). This advantage arises from the presence of expert labeled ground truth. Aortic borders depicted on the modulus images were then superimposed to the velocity images throughout the cardiac cycle to enable blood velocities and flow-rates computation.

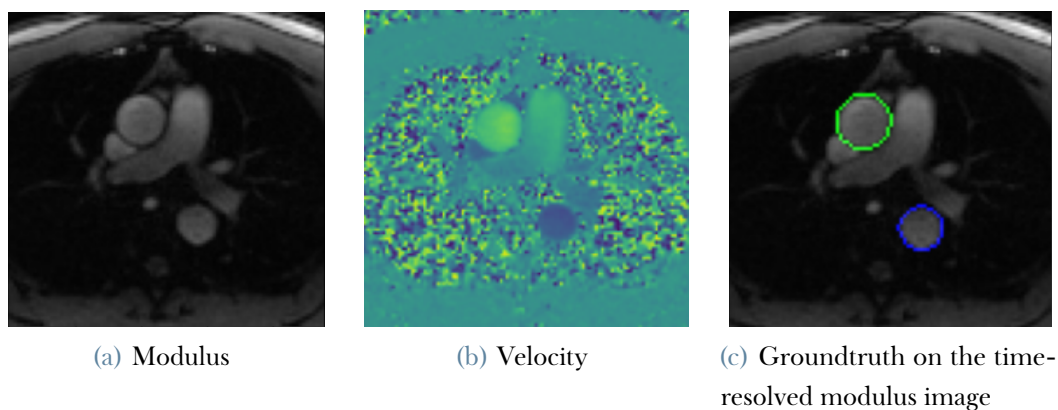


**Figure 3.2:** On the left is the Modulus of the cine MRI image. Centrally positioned is the depiction through plane velocity image. The image on the right is displaying the superposition of the ground truth of the aorta's segmentation laid over the Modulus image, illustrated here on a single phase of the cardiac cycle but achieved on all the time phases.

In terms of numerical aspects, the study encompasses a diverse cohort of 403 patients, collectively contributing to the richness of the dataset. On average, each patient's MRI sequence comprises around 60 modulus/velocity images corresponding to a single cardiac cycle. This significant dataset not only facilitates an in-depth exploration of cardiac dynamics but also permits the identification of patterns, trends, and variations across diverse subjects and temporal dimensions. The data collected is anonymized to protect the privacy of all personal and identifiable information. All patients gave a signed and informed consent regarding the use of their data for clinical research purpose.

In summary, this research project involves a meticulous examination of specialized 2D dynamic MRI images that offer insights into the aortic behavior. By employing the DICOM standard, refining the technique of identifying different arterial sections, and analyzing a substantial number of patient images, the study aims to unveil intricate aspects of cardiac functioning.

## 3.2. Data preprocessing

From the DICOM file, we retrieve the modulus pixel array. For our application, the pixel array should be of type 'float32', chosen for its balance of precision and memory usage. Once we've retrieved the pixel array, a significant consideration is the consistency of image sizes. We aim for each image to be uniform in dimensions. To achieve this, we selected a size of 224x224 pixels for our images.

This dimension is a strategic compromise. On one hand, if the original image is significantly larger than this, reducing its size might mean a potential loss of detail. To address this while still achieving our target size, we crop larger images. But rather than arbitrarily cropping them, we ensure we retain the central portion, which holds the most vital information regarding the aortic sections. On the other hand, there is a practical limitation to consider. Larger images would necessitate a larger and potentially more complex deep learning model, which would be more computationally intensive to train.

Conversely, if an image is smaller than our desired 224x224 dimensions, simply enlarging it might introduce unwanted artifacts or blur. To tackle this, we employ the zero-padding, adding rows and columns of zeros to the image, essentially creating a border. This way, the original image content remains unaltered and centered, but the overall dimensions match our target dimension.

Once the image is resized to the desired dimensions, we perform a min-max normalization to ensure pixel values are standardized and to account for contrast changes between patients. With the image now in the desired size and normalized intensities, the next step is to convert it into a format amenable to deep learning operations. In deep learning, images are typically processed as tensors, which are multi-dimensional arrays. So, we transform our 224x224 image into a tensor, streamlining it for integration into deep learning frameworks and algorithms.

Parallel to processing the primary images, we apply the same transformations to the groundtruth masks. These groundtruth images are vital as they serve as the reference or the "truth" to train and evaluate the developed models. In our case, the groundtruth is a 3D array with dimensions 224x224x3 for each phase of the cardiac cycle. This 3D shape is indicative of the three distinct classes or labels in our dataset: the Background, the Ascending Aorta (AAo), and the Descending Aorta (DAo).

By standardizing our images and their corresponding groundtruths in this manner, we lay the groundwork for efficient and consistent deep learning model training.

In the realm of medical imaging, particularly with DICOM files, there is a process to translate the representation of intensities in the velocity images into actual, real blood velocity values. This translation can be achieved by leveraging specific information found within the DICOM files. Mathematically, this relationship is captured by the equation:

$$\mathbf{V} = \mathbf{m} \times (\mathbf{I} - \mathbf{z}). \quad (3.1)$$

Where  $V$  represents the real velocity in cm/s,  $I$  denotes the pixel value in the DICOM velocity image,  $m$  is the slope and  $z$  is the y-intercept (or the ordinate at the origin) provided into the DICOM information,  $m$  being estimated from the encoding velocity applied by the operator prior to the acquisition.

In our study, it is crucial to ensure a proper division of the dataset for effective training, validation, and testing of our model. We divide the dataset into three distinct sets: training, validation, and testing. Although the split is random, we perform this division only once and maintain this distribution throughout the study. This strategy aims to eliminate the risk of testing on data used for training, which could introduce bias and give an overly optimistic view of the model's performances. By adhering to this approach, we ensure the integrity and reliability of our results.

With the provision of four distinct patient files, we take meticulous care in distributing them evenly across different folders. It is important to highlight that no single folder contains multiple entries of the same patient. This organization ensures that no bias is inadvertently introduced, maintaining the integrity and robustness of our study.

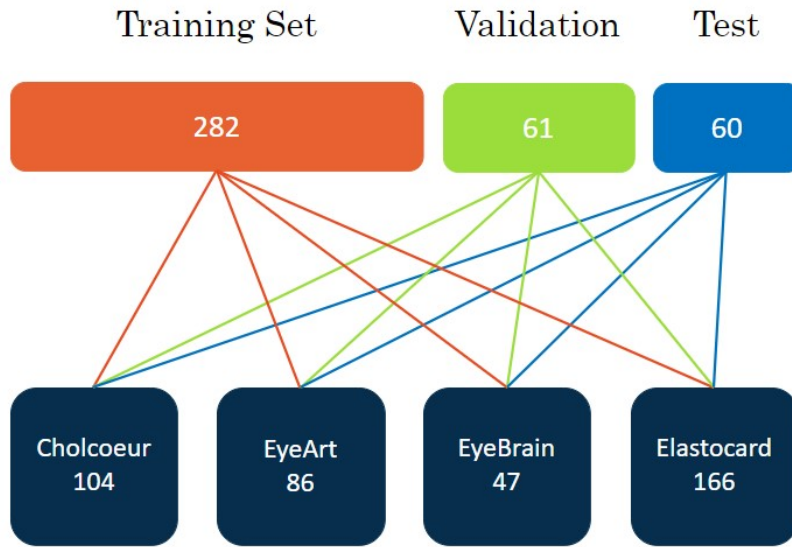


**Figure 3.3:** The files labeled 'Cholcoeur', 'EyeArt', 'EyeBrain', and 'Elastocard' correspond to diverse groups of patients with different arterial status (hypertensive, old, healthy volunteers) and acquired in different centers (Pitié-Salpêtrière Hospital with the cardiac and neuro departments and European Hospital Georges Pompidou with its cardiac department) and on different scanners (Siemens and GE with 1.5 and 3T) . Data from these cohorts are uniformly distributed across the training, validation, and testing sets. These sets comprise 282, 61, and 60 cine MRI images, respectively.

### 3.3. Models

In the subsequent section, we will outline the three primary methodologies that underpin this research. We will discuss their foundational principles, provide insights into our reasons for choosing them, and detail how they were integrated into the study's framework.

#### 3.3.1. Vanilla Method

In our study, we employ an approach termed the "Vanilla Method." This designation stems from our application of a pre-existing algorithm, specifically the UNet++ architecture, a refined variant of the traditional UNet. Our choice of this architecture is grounded in the literature, indicating its superior efficiency for the challenges we address. To expedite our implementation process, we utilize the ready-to-use codebase for this methodology as offered by the Segmentation Models Pytorch (smp) library.

Our deep learning model, crafted using the foundational Vanilla Method, is meticulously

designed, emphasizing the selection of critical parameters to guarantee optimal performance. We commit to a batch size of 16, aiming to guarantee an efficient gradient update during the training stages, optimizing computational resources, and appropriately managing memory overheads. For the loss function, we pick the Cross Entropy Loss, widely used in tasks emphasizing classification due to its ability to precisely quantify the deviation between the model's predictions and actual results.

For optimization, we use the Adam optimizer, known for its adaptability and unmatched efficiency in overseeing model refinements. Complementing this, we set a learning rate of  $1 \times 10^{-4}$ . This rate, in our assessment, achieves the compromise between ensuring fast convergence and negating potential overshooting in the model's learning evolution. To add a layer of protection against the pitfalls of overfitting and to circumvent redundant computations, we embed an early stopping mechanism designed to interrupt the training if there is an absence of performance enhancement over 20 consecutive epochs.

From an architectural standpoint, the Vanilla Method pivots on the 'vgg19\_bn' base. Our affinity for this framework is inspired by the inherent stability of the VGG19 model, further augmented by the integration of batch normalization. Aiming to fast-track the training phase and equip the model with a solid foundational grasp, we initialize the encoder segment of our architecture with weights pretrained on the vast ImageNet dataset.

### 3.3.2. ROI-centered Method

Our primary aim is to boost both the efficiency and accuracy of our image analysis by concentrating on the most prominent sections of the cine MRI images. Understanding that not every segment of an image sequence carries valuable insights, we prioritize refining these specific portions to optimize our analysis.

In our initial approach, we deploy the Vanilla UNet model to process the first five images from the cine MRI sequence. By analyzing these images and aggregating their predictions, we identify areas of the images that contain the most relevant data.

Leveraging these insights, we design a cropping strategy. We pinpoint the extreme points from our aggregated predictions and then calculate the midpoint between them. This central point serves as the foundation of our cropping process. To maintain consistency, each image in the sequence undergoes cropping to a standard dimension of 128x128 pixels. We ensure that the center of each cropped area aligns with the previously determined midpoint.

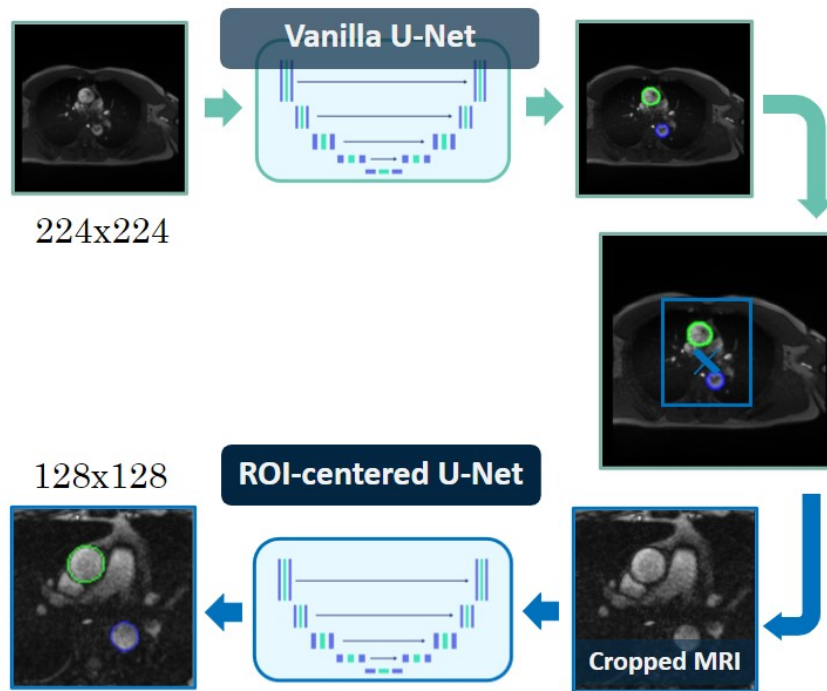


**Figure 3.4:** Here is the schematic representation of the ROI-centered method. Initially, the original image undergoes processing by the Vanilla method. Based on the predictions generated, an ROI is identified, and subsequently, the image is cropped to match this ROI. The cropped image is then directed into another instance of the UNet++ architecture for a segmentation refinement.

Next, we subject the cropped images to further analysis, using the UNet++ architecture. During this phase, most of our hyperparameters stay consistent with those from the earlier model. However, due to the reduced dimensions of the cropped images, we adjust the batch size to 32, up from the original 16.

This refined methodology is called ROI-centered method in our the following parts of the thesis. Being centered around specific regions of interest within the cine MRI images, this method holds the potential for delivering faster and more precise results.

### 3.3.3. Ascending Aorta and Descending Aorta-centered Method

To further broaden our investigative scope and enhance precision, we formulated a third method that delves deeper into the principles established by our previous approach. Rather than confining our analysis to a singular region of interest encompassing both the ascending and descending aorta, we've differentiated our approach. Specifically, we delineated two distinct regions of interest: one tailored for the Ascending Aorta (AAo) and another for the

Descending Aorta (DAo).

The mechanics of this method mirror the strategies we have discussed earlier. We initiate by applying the Vanilla UNet++ to the first five images of the cine MRI sequence. These preliminary images provide an aggregate of predictions for each aorta section. The center position of each aorta is then identified based on these aggregated predictions.

The subsequent step involves cropping the cine MRI images, tailored to each aorta's dimensions. The cropping for the AAo is set at 96x96 pixels, while the DAo is cropped to a dimension of 32x32 pixels. This specificity in size selection ensures that the entirety of each aorta section is captured without resorting to a larger crop size, which would invariably intensify computational demands.

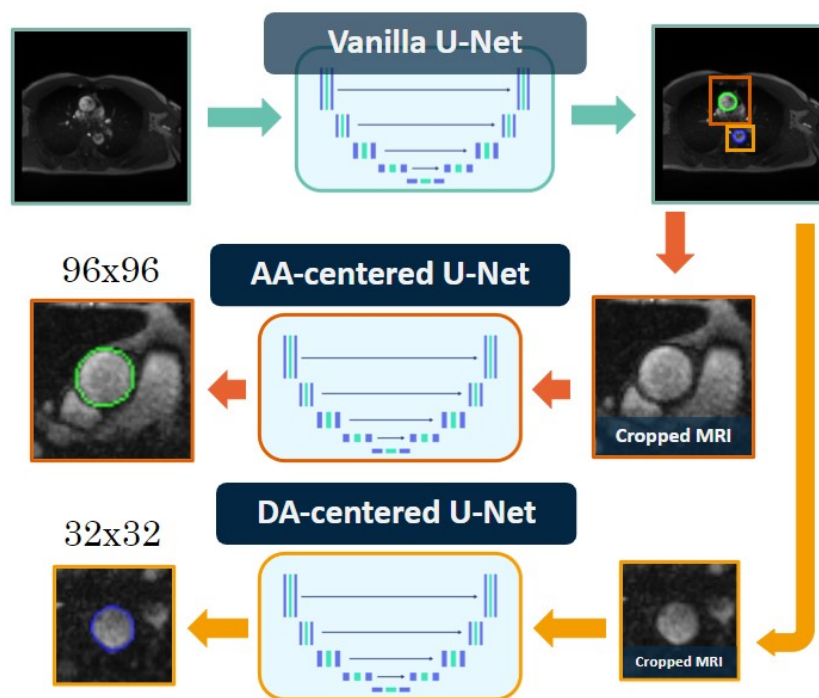


Figure 3.5: Displayed below is the schematic representation of the AAo and DAo-centered method. To begin, the original image is subjected to processing through the Vanilla method. Predictions generated from this initial step are then used to pinpoint ROI for both the Ascending Aorta (AAo) and the Descending Aorta (DAo). Following this, the image is cropped to align with these ROIs. Subsequently, each of these cropped images is directed into separate instances of the UNet++ architecture, facilitating a more refined and specialized segmentation process.

The process of hyperparameter tuning for this method mirrors the configurations we employed for the ROI-centered approach. In our results, we refer to this innovative technique

as the AAo and DAo-centered method, symbolizing its dual focus on both the ascending and descending aorta sections.

Our third method brings a targeted advancement in the segmentation of the aorta in dynamic MRI images, building logically upon the foundations laid by the Vanilla Method. By distinctly focusing on two separate regions of interest - the ascending and descending aorta sections - it facilitates a more nuanced analysis compared to approaches that treat this region as a single entity.

A noteworthy strategy here is the implementation of different cropping dimensions for each section, which serves to maintain a balance between computational efficiency and the encompassment of each aorta section in its entirety. Moreover, the initial use of the Vanilla UNet++ in analyzing the first few cine MRI sequences helps in setting a solid base for precise segmentation through the refined identification of central positions for each aorta section.

This AAo and DAo-centered approach, therefore, offers a thoughtful refinement to existing techniques, introducing a level of specificity that aims to enhance precision without significantly amplifying computational demands. It represents a step forward in the ongoing efforts to improve the accuracy and efficiency of aorta segmentation in dynamic MRI imagery.

## 3.4. Metrics Used

### 3.4.1. Cross-entropy Loss

Evaluating our model's performance during training is crucial. A well-chosen metric not only gauges accuracy but also guides model optimization. For this purpose, we've selected Cross-entropy loss.

Cross-entropy loss, often just termed cross-entropy, measures the dissimilarity between two probability distributions: actual and predicted. It evaluates how closely a model's predicted probability distribution aligns with the true data distribution. Given by

$$H(p, q) = - \sum p(x) \log(q(x)),$$

$p(x)$  is the true probability of event  $x$ , while  $q(x)$  is its predicted probability.

For binary classification, this simplifies to:

$$H(p, q) = -p \log(q) - (1 - p) \log(1 - q),$$

where  $p$  represents the true class (0 or 1), and  $q$  is the predicted probability for the given class.

The unique aspect of cross-entropy is its penalization: if predictions deviate from true labels, the loss increases, nudging the model toward better predictions. This metric also aligns with the goal of Maximum Likelihood Estimation, making it ideal for deep learning classification tasks. However, its limitations include unsuitability for regression and potential issues in highly imbalanced datasets [22, 32].

In essence, cross-entropy evaluates differences between probability distributions and is commonly used in deep learning classification due to its effective penalization and ties to Maximum Likelihood Estimation.

### 3.4.2. Dice

After training, when evaluating or testing our model, it is vital to use a distinct metric than the metric used for model optimization. Therefore, for a more objective assessment, we will employ separate metrics.

The Dice coefficient is a statistical metric that provides a quantitative assessment of the similarity or overlap between two sets. In the context of segmentation tasks, it measures the overlap between the predicted segmentation mask ( $A$ ) and the ground truth mask ( $B$ ) [79].

To calculate the Dice coefficient, we consider the number of pixels in both the predicted and ground truth masks and the number of overlapping pixels between them. The formula for calculating the Dice coefficient is therefore:

$$Dice = \frac{2 * |A \cap B|}{|A| + |B|}. \quad (3.2)$$

where  $|A|$  and  $|B|$  represent the sizes (number of pixels) of the corresponding masks, and  $|A \cap B|$  denotes the number of pixels that are both in the predicted and ground truth masks [79].

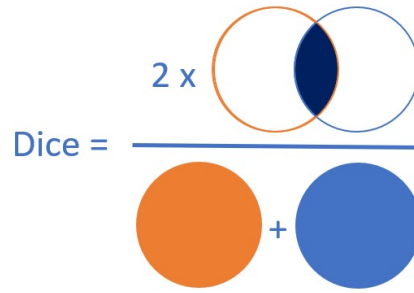


Figure 3.6: Visual representation of the Dice metric, the circles represent the predicted and ground truth masks.

By multiplying the intersection of the masks by 2 and dividing it by the sum of the sizes of both masks, the Dice coefficient provides a normalized measure of overlap between the two masks. This normalization ensures that the coefficient ranges between 0 and 1, where 0 indicates no overlap (complete dissimilarity) and 1 indicates a perfect match (complete similarity) [23].

It is important to note that the Dice coefficient has limitations. For instance, it doesn't differentiate between different types of errors (e.g., false positives and false negatives). Also, the Dice coefficient doesn't consider spatial information or variations in shape, and it treats all pixels equally without considering their relative importance within the segmented region [56].

Researchers and practitioners frequently use the Dice coefficient in conjunction with other metrics. As a result, we present our findings using both the Dice Score and the Hausdorff distance [79].

### 3.4.3. Hausdorff

The Hausdorff distance or Hausdorff metric is a measure of dissimilarity between two sets of points or regions. In the context of segmentation tasks, the Hausdorff metric quantifies the maximum distance between the predicted segmentation mask and the ground truth mask, considering all points in one mask and finding the closest point in the other mask [6, 26].

To calculate the Hausdorff distance, we consider two sets of points: set A representing the predicted segmentation mask and set B representing the ground truth mask. The Hausdorff distance is defined as:

$$H(\mathbf{A}, \mathbf{B}) = \max(\mathbf{h}(\mathbf{A}, \mathbf{B}), \mathbf{h}(\mathbf{B}, \mathbf{A})). \quad (3.3)$$

where  $h(A, B)$  represents the directed Hausdorff distance from set A to set B, and  $h(B, A)$  represents the directed Hausdorff distance from set B to set A.

The directed Hausdorff distance from set A to set B is defined as:

$$h(\mathbf{A}, \mathbf{B}) = \max(\min(d(\mathbf{a}, \mathbf{b}) | \mathbf{b} \in \mathbf{B}) | \mathbf{a} \in \mathbf{A}). \quad (3.4)$$

where  $d(a, b)$  represents the Euclidean distance between point a in set A and point b in set B [26].

By considering the maximum value between the directed Hausdorff distances in both directions, the Hausdorff distance captures the maximum dissimilarity or distance between the predicted and ground truth masks.

The Hausdorff metric is commonly used in segmentation tasks to measure the dissimilarity or error between the predicted and ground truth segmentations. It provides a single value that represents the maximum discrepancy between the two masks, allowing for a quantitative assessment of the quality of the segmentation. The Hausdorff distance is particularly useful when there is a need to evaluate the quality of segmentation in terms of spatial correspondence [26, 36].

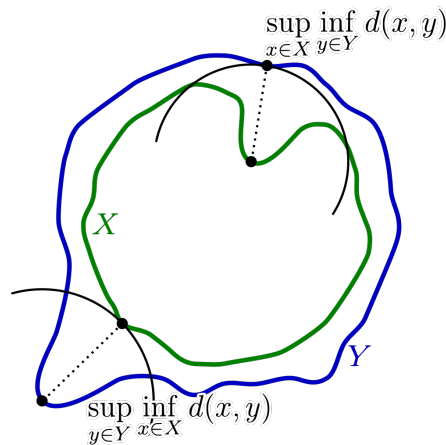


Figure 3.7: Visual representation of the Hausdorff metric between a ground truth and predicted region of interest [71].

It is important to note that the Hausdorff metric is sensitive to outliers or isolated points and is affected by the presence of noise or small local misalignments between the evaluated masks [26].

### 3.4.4. Mean Absolute Error and Mean Squared Error

In addition to accuracy measures, assessing computational speed is crucial, especially for the aorta section. Therefore, we've incorporated two metrics to evaluate our model's ability to accurately quantify blood flow velocity within the ascending and descending aorta: the Mean Absolute Error and Mean Squared Error.

Mean Absolute Error (MAE) quantifies the average of the absolute differences between the predicted and actual values. It is mathematically represented as:

$$\text{MAE} = \frac{1}{n} \sum_{i=1}^n |y_i - \hat{y}_i|$$

where  $n$  denotes the number of observations,  $y_i$  represents the actual value for the  $i$ -th observation, and  $\hat{y}_i$  is its predicted value. The primary appeal of MAE is its straightforward interpretation, as it gives a direct indication of the average magnitude of errors between predicted and actual values, without accounting for their direction. A smaller MAE suggests a model's predictions are closely aligned with the actual values [86].

Transitioning to Mean Squared Error (MSE), this metric computes the average of the squared differences between the predicted and actual values, and can be expressed as:

$$\text{MSE} = \frac{1}{n} \sum_{i=1}^n (y_i - \hat{y}_i)^2$$

The distinct feature of MSE is its emphasis on larger errors due to the squaring operation. This means it penalizes larger discrepancies between actual and predicted values more significantly than MAE. As a result, MSE is particularly sensitive to outliers and may not always provide a straightforward understanding of performance since the errors are squared [13].

A defining difference between MAE and MSE lies in their treatment of errors: MAE offers a linear penalty for each error, while MSE gives a quadratic one. This distinction implies that if large errors are especially undesirable, MSE might be the metric of choice. Conversely, if the goal is to obtain an uncomplicated average error magnitude without excessive influence from outliers, MAE might be more appropriate [13, 86].

In deep learning applications, the choice between MAE and MSE hinges on the error distribution and the study's specific objectives, guiding researchers and practitioners to make informed decisions based on their requirements.

# 4 | Results

## 4.1. Results

In our study, we evaluate the performances of each developed model based on various criteria to determine the most suitable model for our aortic segmentation task from dynamic MRI images. From a computational standpoint, all methods demonstrate efficiency, with each taking less than 2 seconds to process a cine MRI for a patient, a duration deemed acceptable for our application.

The three methods have been applied to the test set presented in Figure 3.3. The results are categorized and presented based on two primary metrics: Dice Score and Hausdorff distance in pixels. For each metric, we'll provide detailed tables showcasing the median, the first quartile, and the third quartile values. Accompanying these tables are box-plots that give a comparative view of the different methods tested.

The cropping carried out for both the ROI-centered method and the AAO and DAO-centered method involves placing the cropped regions back onto the original image. This allows for a meaningful comparison of the three methods.

Of particular note is the representation of the p-value in our analysis. This statistical measure helps in understanding the statistical significance of our findings. In the box-plots, a single star denotes a p-value in the range (0.01, 0.05], two stars represent a p-value in the range (0.001, 0.01], and three stars indicate a p-value of 0.001 or less.

By providing these detailed statistics and visual representations, we aim to offer a comprehensive view of our model evaluations, facilitating an informed selection of the best segmentation model.

Looking at Table 4.1 and Figure 4.1, we can clearly see that the AAO and DAO-centered Method has the best Dice Score.

Method used	Metrics			
	AAo Dice	DAo Dice	AAo Hausdorff	DAo Hausdorff
Vanilla	0.972 [0.960; 0.978]	0.951 [0.937; 0.957]	<b>1.10 [1.01; 1.17]</b>	<b>1.05 [1.01; 1.11]</b>
ROI-centered	0.970 [0.950; 0.973]	0.947 [0.930; 0.957]	1.21 [1.15; 1.33]	1.19 [1.09; 1.23]
AAo and DAo-centered	<b>0.976 [0.963; 0.980]</b>	<b>0.956 [0.946; 0.965]</b>	<b>1.10 [1.01; 1.16]</b>	<b>1.08 [1.04; 1.12]</b>

**Table 4.1:** The results displayed cover the entire test set (Figure 3.3). They provide insights into both the Dice score and the Hausdorff distance for the AAo and the DAo. Each result is formatted as Median[First Quartile; Third Quartile]

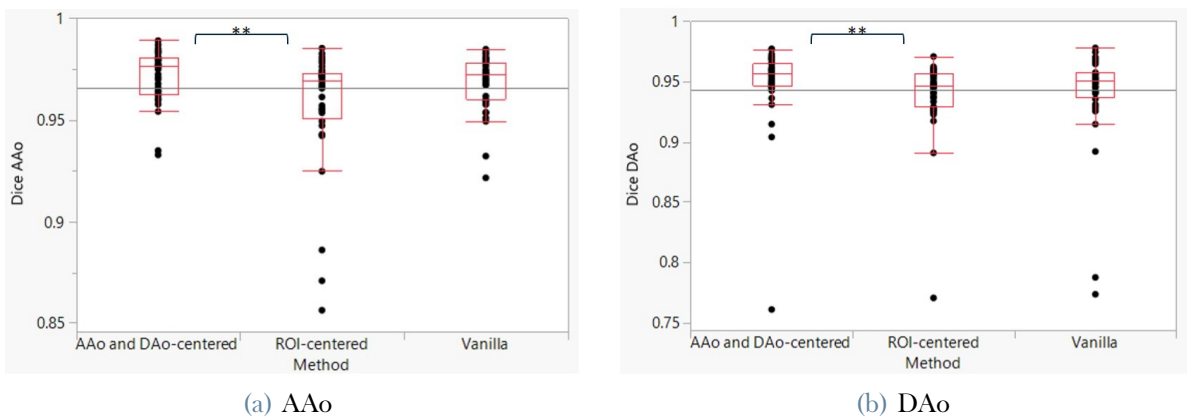


**Figure 4.1:** The figure provides a box-plot representation of the Dice Score based on the entire test set. The significance of the differences, denoted by stars, lies within the interval (0.001, 0.01].

Level	- Level	Score Mean Difference	Std Err Dif	Z	p-Value
Vanilla	ROI-centered	7.8611	4.932883	1.59361	0.1110
Vanilla	AAo and DAo-centered	-6.8056	4.932883	-1.37963	0.1677
ROI-centered	AAo and DAo-centered	-13.0833	4.932883	-2.65227	<b>0.0080*</b>

**Figure 4.2:** Wilcoxon Significance computation Dice AAo - To compare the efficacy of the Vanilla, ROI-centered, and AAo and DAo-centered methods, we computed the Wilcoxon significance through an analysis encompassing score mean differences, standard error of differences, Z-scores, and p-values.

Level	- Level	Score Mean Difference	Std Err Dif	Z	p-Value
Vanilla	ROI-centered	4.1389	4.932883	0.83904	0.4014
Vanilla	AAo and DAo-centered	-7.6944	4.932883	-1.55983	0.1188
ROI-centered	AAo and DAo-centered	-12.7500	4.932883	-2.58470	0.0097*

Figure 4.3: Wilcoxon Significance computation Dice DAo - Comparison of the effectiveness of the Vanilla, ROI-centered, and both AAO and DAo-centered approaches. We conducted a Wilcoxon significance analysis, taking into account factors such as score mean differences, standard error of differences, Z-scores, and p-values.

From Figure 4.1 Figure 4.2 and Figure 4.3, the p-value indicates that there is a notable difference in results between the AAO and DAo-centered method and the ROI-centered method, for both the Aortic sections.

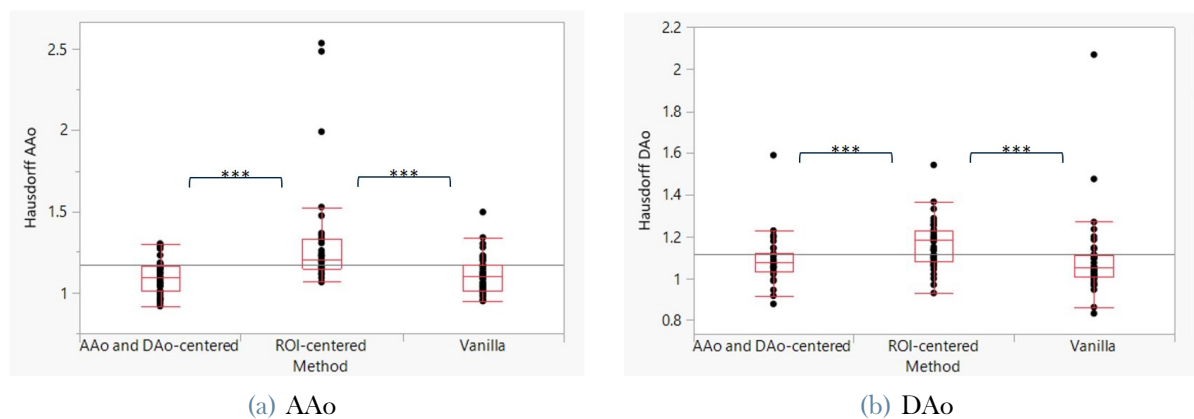


Figure 4.4: The figure displays several box-plots illustrating the Hausdorff distance derived from the complete test set. Differences marked with stars indicate a significance level of less than 0.001.

Level	- Level	Score Mean Difference	Std Err Dif	Z	p-Value
ROI-centered	AAo and DAo-centered	22.5278	4.932883	4.56686	<.0001*
Vanilla	AAo and DAo-centered	0.6389	4.932883	0.12952	0.8969
Vanilla	ROI-centered	-21.9167	4.932883	-4.44297	<.0001*

Figure 4.5: Wilcoxon Significance computation Hausdorff AAO - Computation of the Score Mean differences, Standard Error of Differences, z-scores and p-values comparing the Vanilla, the ROI-centered and the AAO and DAo-centered method.

Level	- Level	Score Mean Difference	Std Err Dif	Z	p-Value
ROI-centered	AAo and DAo-centered	16.9167	4.932883	3.42937	0.0006*
Vanilla	AAo and DAo-centered	-3.4722	4.932883	-0.70389	0.4815
Vanilla	ROI-centered	-16.9167	4.932883	-3.42937	0.0006*

Figure 4.6: Wilcoxon Significance computation Hausdorff DAo - Calculation of score mean differences, standard error of differences, z-scores, and p-values in a comparative analysis of the Vanilla, ROI-centered, and AAo and DAo-centered methods.

In both aortic sections, Figure 4.4, we observe a notable difference  $p\text{-value} < 0.001$  between the AAo and DAo-centered method and the ROI-centered method, as well as between the Vanilla and ROI-centered method.

To gauge the efficacy of our model, we will benchmark the best-performing iteration of the AAo and DAo-centered method against the current state-of-the-art, represented by the findings of Bai et al. [8], Biasioli et al. [12], and Hann et al. [35]. This comparison will employ the Dice Score metric, as it is the sole metric universally utilized across the studies we intend to reference for this analysis.

Method used	Average Dice Score	
	AAo	DAo
Bai et al.	0.960	0.953
Hann et al.	0.967	0.966
Biasioli et al.	0.97	0.98
AAo and DAo-centered	0.976	0.956

Table 4.2: State of the Art Dice Score comparison - The table illustrates a comparison between the AAo and DAo method and the current state-of-the-art techniques, presenting Dice Scores to three significant figures, except for the method developed by Biasioli et al., which provides only two.

The AAo and DAo-centered method appears to excel notably in achieving a high Dice Score for the ascending aorta, while demonstrating moderate precision for the descending aorta. Meanwhile, the data from Biasioli et al. presents a peculiar scenario; the limited use of two significant figures inhibits a conclusive analysis for the ascending aorta. Furthermore, it is non-intuitive to observe a higher Dice Score for the descending aorta given its smaller

sectional area — a trait generally associated with lower scores, as evidenced in both this study and others referenced.

## 4.2. Results according to the size of the Ascending Aorta

In our study, we aim to enhance the software’s ability to identify stiff and dilated aortas. Therefore, it’s crucial to assess how effectively our methods work on data from both healthy individuals and those with stiff aortas. Therefore we tested our results on the 50 healthy subjects of the test sets and on the 10 other subjects presenting a Large AAo. Each 2D cine MRI consists of an average of 60 images. Thus, the test set actually comprises 3,000 2D images for healthy subjects and 600 2D images for patients with a dilated aorta.

Method used	Set Considered	
	Healthy Aorta	Large AAo
Vanilla	0.973 [0.962; 0.980]	<b>0.983 [0.972; 0.989]</b>
ROI-centered	0.968 [0.952; 0.976]	0.979 [0.963; 0.981]
AAo and DAo-centered	<b>0.977 [0.964; 0.984]</b>	<b>0.983 [0.981; 0.986]</b>

**Table 4.3:** AAo Dice Score - The table showcases a comparison of the deep learning methods according to the aortic size. The AAo Dice Score is presented in the format Median[First Quartile; Third Quartile].

In Table 4.3, it is observable that the AAo and DAo-centered method yields superior results for the Healthy dataset while matching the performance of the Vanilla method for the dataset with Large AAo. Nevertheless, the Dice Scores appear to be elevated for the Large AAo dataset.

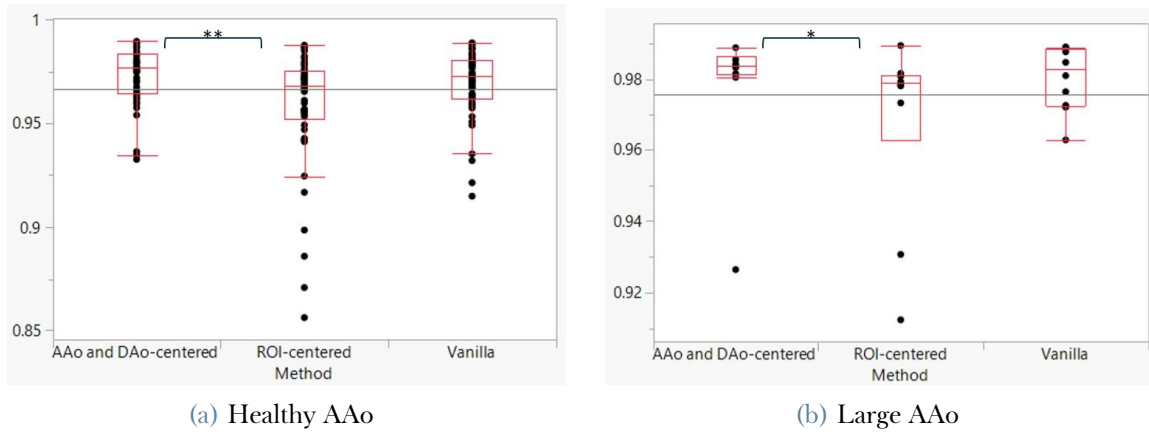


**Figure 4.7:** AAO Dice Score - The figure presents box-plots that depicts the Dice score for both the Healthy Aorta dataset and the Large AAO dataset. The stars highlighting differences suggest a significance level between 0.001 and 0.01 for the Healthy AAO, and between 0.01 and 0.05 for the Large AAO.

In Figure 4.7 and Figure 4.8, there's a notable p-value distinction between the AAO and DAo-centered method and the ROI-centered method.

Method used	Set Considered	
	Healthy Aorta	Large AAO
Vanilla	0.953 [0.940; 0.972]	0.977 [0.950; 0.981]
ROI-centered	0.950 [0.933; 0.960]	0.964 [0.939; 0.972]
AAo and DAo-centered	<b>0.958 [0.947; 0.971]</b>	<b>0.977 [0.970; 0.984]</b>

**Table 4.4:** DAo Dice Score - The table offers a side-by-side evaluation of the Deep Learning techniques based on aortic dimensions. DAo Dice Scores are formatted as Median[First Quartile; Third Quartile].

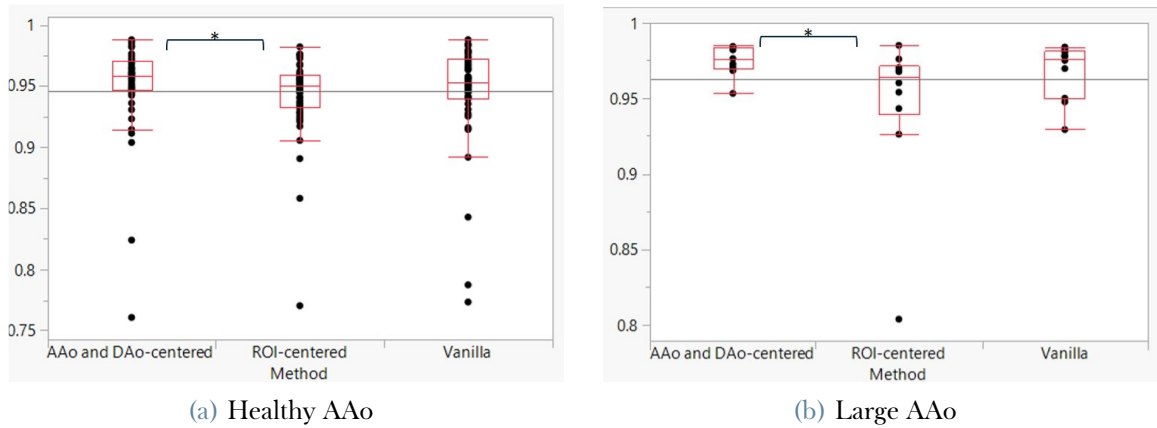


**Figure 4.8:** DAAo Dice Score - The figure illustrates box-plots of the Dice scores for the Healthy Aorta and Large AAO datasets. The stars marking distinctions indicate significance levels ranging from 0.01 to 0.05.

Method used	Set Considered	
	Healthy Aorta	Large AAO
Vanilla	<b>1.10 [1.02; 1.18]</b>	1.27 [1.21; 1.49]
ROI-centered	1.20 [1.15; 1.33]	1.49 [1.34; 1.97]
AAo and DAAo-centered	<b>1.10 [1.00; 1.17]</b>	1.34 [1.16; 1.62]

**Table 4.5:** AAO Hausdorff distance - This table provides a comparative assessment of the Deep Learning approaches according to aortic size. AAO Hausdorff distance are formatted as Median[First Quartile; Third Quartile]

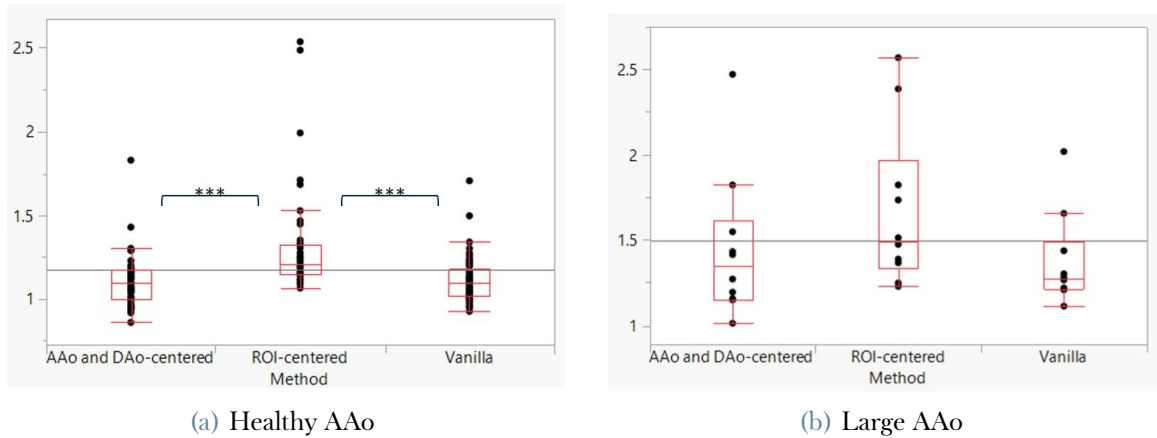


**Figure 4.9:** AAO Hausdorff distance - The figure illustrates box-plots of the Hausdorff distance for each method considered applied to the Healthy AAO and Large AAO datasets. The stars marking distinctions indicate significance levels lower than 0.001.

From Table 4.5 and Figure 4.9, it is clear that a significant difference exists between the Vanilla and ROI-centered methods as well as the ROI-centered methods and the AAO and DAo-centered method, in the context of a Healthy AAO, with the p-values being below 0.001.

Method used	Set Considered	
	Healthy Aorta	Large AAO
Vanilla	1.04 [0.99; 1.11]	1.13 [1.02; 1.21]
ROI-centered	1.16 [1.07; 1.23]	1.24 [1.20; 1.34]
AAo and DAo-centered	1.06 [1.00; 1.12]	1.09 [1.01; 1.21]

**Table 4.6:** DAo Hausdorff distance - This table offers a comparison of Deep Learning methodologies based on aortic size. The DAo Hausdorff distances are represented in the format: Median[First Quartile; Third Quartile].

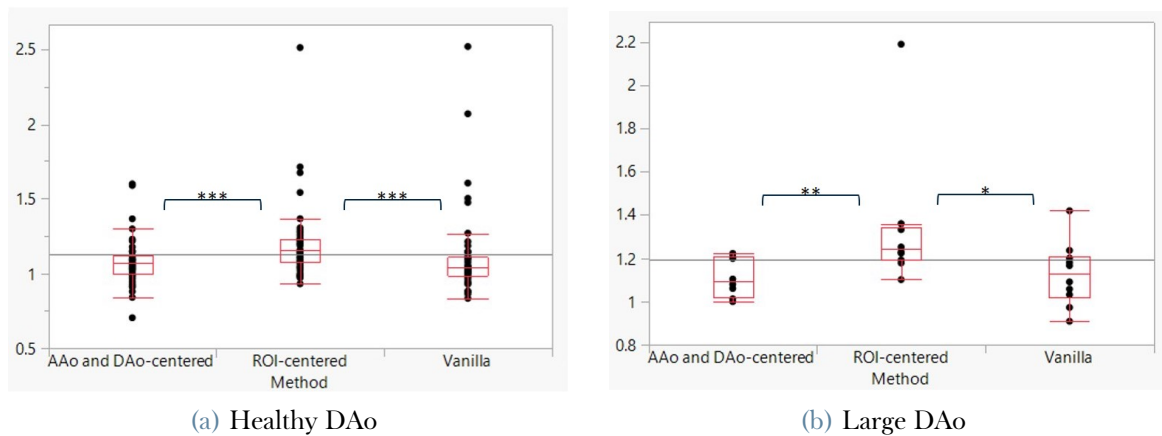


**Figure 4.10:** DAo Hausdorff distance - The figure displays box-plots representing the Hausdorff distance for each method when applied to both the Healthy DAo and Large DAo datasets. Significance levels, indicated by stars, are as follows: one star corresponds to a p-value between 0.01 and 0.05, two stars denote a p-value between 0.001 and 0.01 and three stars represent a p-value lower than 0.001.

From Table 4.6 and Figure 4.10, we observe that significant differences exist between the Vanilla and ROI-centered methods, and also between the ROI-centered methods and the AAO and DAo-centered method. These differences are more pronounced for the Healthy AAO, as indicated by the notably lower p-values.

### 4.3. Results according to the blood flow velocity computation

A key part of our study is measuring the flow velocity in the aorta. To give a complete view, we also need to look at how our different methods compare based on this measurement which is often used by clinicians to quantify arterial function, a degree of stenosis, and cardiac function and output.

Method used	Mean Absolute Error	
	Ascending Aorta	Descending Aorta
Vanilla	2.77 [2.28; 4.34]	5.69 [3.58; 7.85]
ROI-centered	3.40 [2.47; 5.47]	8.20 [4.79; 12.46]
AAo and DAo-centered	<b>2.64 [1.75; 3.74]</b>	<b>5.58 [3.52; 7.36]</b>

**Table 4.7:** Mean Absolute Error - This table compares the Deep Learning methodologies based on the computation of the blood flow velocity in cm/s in the aorta from the MRI images. The Mean Absolute Error is shown in the format: Median[First Quartile; Third Quartile]

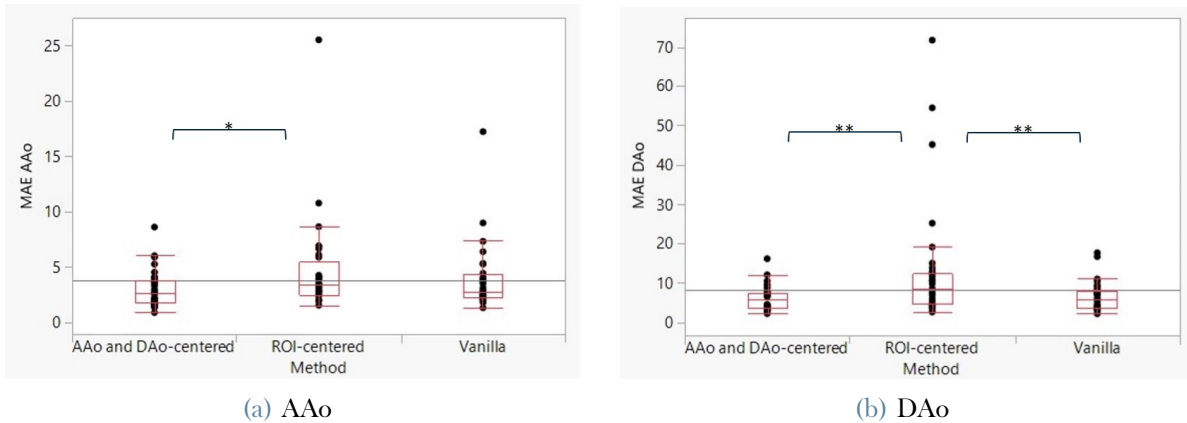


**Figure 4.11:** Mean Absolute Error - The figure showcases box-plots that depict the MAE of the calculated blood flow velocity in cm/s for each method across the full dataset. The presence of stars signifies significance levels: a single star represents a p-value ranging from 0.01 to 0.05, and two stars correspond to a p-value ranging from 0.001 to 0.01.

Level	- Level	Score Mean Difference	Std Err Dif	Z	p-Value
ROI-centered	AAo and DAo-centered	11.8611	4.932883	2.40450	0.0162*
Vanilla	AAo and DAo-centered	6.9167	4.932883	1.40216	0.1609
Vanilla	ROI-centered	-5.9722	4.932883	-1.21070	0.2260

**Figure 4.12:** Wilcoxon Significance computation MAE Velocity AAO - Evaluating the Vanilla, ROI-centered, and AAO and DAo-centered methods through the determination of score mean differences, standard error of differences, z-scores, and p-values.

Level	- Level	Score Mean Difference	Std Err Dif	Z	p-Value
ROI-centered	AAo and DAo-centered	15.3611	4.932883	3.11402	0.0018*
Vanilla	AAo and DAo-centered	3.1389	4.932883	0.63632	0.5246
Vanilla	ROI-centered	-13.1944	4.932883	-2.67479	0.0075*

Figure 4.13: Wilcoxon Significance computation MAE Velocity DAo - Evaluation of the Vanilla, ROI-centered, and AAo and DAo-centered methods by determining the score mean differences, standard error of differences, z-scores, and p-values.

The MAE values presented in Table 4.7, Figure 4.11, Figure 4.12 and Figure 4.13 highlight the superiority of the AAo and DAo-centered Method over the ROI-centered method, especially for the DAo flow velocity quantification. Additionally, in the case of the DAo, a notable distinction exists between the Vanilla method and the ROI-centered method.

In our analysis, we have incorporated the MSE as a pivotal metric. The rationale behind this choice is the inherent property of MSE to heavily penalize larger errors. This ensures that any significant deviations in our predictions are promptly highlighted, thus providing a rigorous assessment of the model's accuracy and reliability.

Method used	Mean Squared Error	
	Ascending Aorta	Descending Aorta
Vanilla	14.3 [9.5; 45.1]	56.6 [26.6; 138.4]
ROI-centered	23.1 [13.0; 87.3]	127.0 [48.3; 287.6]
AAo and DAo-centered	13.4 [5.5; 38.1]	58.9 [24.8; 100.6]

Table 4.8: Mean Squared Error - This table contrasts various Deep Learning techniques by assessing the computation of blood flow velocity in cm/s from MRI images. The Mean Squared Error is displayed as: Median[First Quartile; Third Quartile].

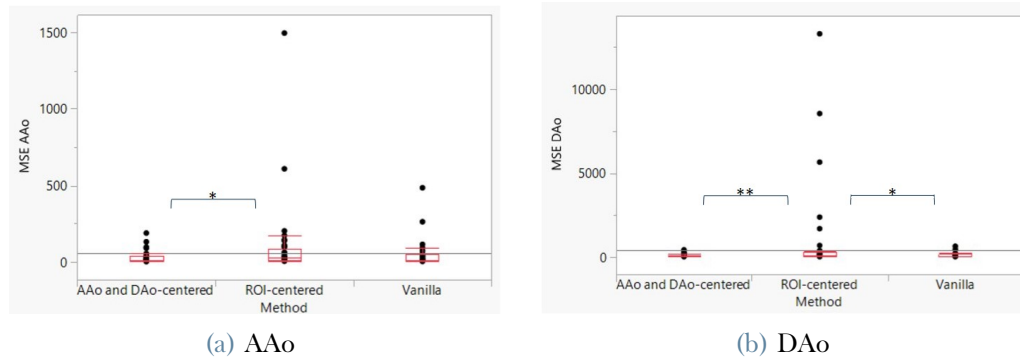


**Figure 4.14:** Mean Squared Error - The figure showcases box-plots that depict the MSE of the calculated blood flow velocity in cm/s for each method across the full dataset. The presence of stars signifies significance levels: a single star represents a p-value ranging from 0.01 to 0.05, and two stars correspond to a p-value ranging from 0.001 to 0.01.

Level	- Level	Score Mean Difference	Std Err Dif	Z	p-Value
ROI-centered	AAo and DAo-centered	11.7500	4.932883	2.38197	0.0172*
Vanilla	AAo and DAo-centered	5.9722	4.932883	1.21070	0.2260
Vanilla	ROI-centered	-7.5278	4.932883	-1.52604	0.1270

**Figure 4.15:** Wilcoxon Significance computation MSE Velocity AAO - Computation of the Significance between the Vanilla, ROI-centered, and AAO and DAO-centered methods through the determination of score mean differences, standard error of differences, z-scores, and p-values.

Level	- Level	Score Mean Difference	Std Err Dif	Z	p-Value
ROI-centered	AAo and DAo-centered	14.5278	4.932883	2.94509	0.0032*
Vanilla	AAo and DAo-centered	2.8056	4.932883	0.56875	0.5695
Vanilla	ROI-centered	-12.5278	4.932883	-2.53965	0.0111*

**Figure 4.16:** Wilcoxon Significance computation MSE Velocity DAO - Evaluation of the Significance between the Vanilla, ROI-centered, and AAO and DAO-centered methods through the determination of score mean differences, standard error of differences, z-scores, and p-values.

As we can see on Table 4.8, Figure 4.14, Figure 4.15 and Figure 4.16 Using the MSE metric, we arrive at conclusions that align closely with those derived from the MAE metric.

The disparity between the Vanilla method and the ROI-centered method appears more pronounced in the context of the DAo.

#### 4.4. Effects of Manufacturer and magnetic field strength

Having gathered sufficient results to determine the optimal model, we can investigate whether there is a connection between the results and both the MRI manufacturers and the magnetic fields in use. The distribution of MRI machines within the test set is detailed in Figure 4.9.

In this comparative analysis, we will exclusively present the Dice score, as the Hausdorff metric in pixels is pertinent for evaluating diverse methods applied to identical data, whereas it does not contribute to the assessment of image quality differences resulting from varied image captures and resolutions.

Manufacturer	Magnetic Field Strength	
	1.5 T	3 T
GE Medical Systems	13	11
Siemens	28	8

Table 4.9: Distribution of MRI machines in the test set based on the manufacturer and magnetic field strength.

From Tables 4.10 and 4.11, it is evident that the most favorable results are achieved with the GE Medical Systems MRI machine that uses a 3T magnetic field. It is important to note that due to the unbalance and the relatively small size of the test dataset, we can make observations but should refrain from drawing definitive conclusions. Furthermore, in both the cases of AAo and DAo, we can observe that the AAo and DAo-centered method delivers the highest Dice scores.

Manufacturer	Magnetic Field	Method used	Median [1st;3rd quartile]
GE Medical Systems	1.5 T	Vanilla	0.972 [0.964; 0.981]
		ROI-centered	0.960 [0.941; 0.978]
		AAo and DAo-centered	0.979 [0.972; 0.981]
	3 T	Vanilla	<b>0.986 [0.984; 0.989]</b>
		ROI-centered	<b>0.980 [0.977; 0.984]</b>
		AAo and DAo-centered	<b>0.987 [0.983; 0.989]</b>
Siemens	1.5 T	Vanilla	0.972 [0.960; 0.979]
		ROI-centered	0.969 [0.943; 0.974]
		AAo and DAo-centered	0.976 [0.963; 0.982]
	3 T	Vanilla	0.972 [0.962; 0.977]
		ROI-centered	0.969 [0.958; 0.973]
		AAo and DAo-centered	0.976 [0.964; 0.980]

Table 4.10: AAo Dice score according to the MRI machines in the test set based on the manufacturer and magnetic field strength. The results are in the format Median[First Quartile; Third Quartile].

Manufacturer	Magnetic Field	Method used	Median [1st;3rd quartile]
GE Medical Systems	1.5 T	Vanilla	0.973 [0.947; 0.978]
		ROI-centered	0.952 [0.935; 0.957]
		AAo and DAo-centered	0.970 [0.954; 0.983]
	3 T	Vanilla	<b>0.979 [0.961; 0.984]</b>
		ROI-centered	<b>0.974 [0.937; 0.976]</b>
		AAo and DAo-centered	<b>0.982 [0.975; 0.985]</b>
Siemens	1.5 T	Vanilla	0.949 [0.937; 0.956]
		ROI-centered	0.946 [0.934; 0.954]
		AAo and DAo-centered	0.956 [0.946; 0.962]
	3 T	Vanilla	0.952 [0.932; 0.967]
		ROI-centered	0.956 [0.926; 0.960]
		AAo and DAo-centered	0.962 [0.947; 0.971]

Table 4.11: DAo Dice score results for MRI machines in the test set, categorized by manufacturer and magnetic field strength. Scores are presented as Median[First Quartile; Third Quartile].

## 5 | Discussion

This study aims to comprehensively evaluate three distinct approaches for aorta segmentation from cine MRI data: the Vanilla method, the ROI-centered method, and the AAo and DAo-centered method. The central focus of this investigation is to ascertain the most suitable method by conducting a meticulous process of evaluation and comparison.

In the initial phase, we are currently assessing the performance of each method across the entire test set. Notably, the AAo and DAo-centered method exhibits a substantial contrast in terms of Dice Score when compared to the ROI-centered method. Moreover, both the Vanilla and AAo and DAo-centered methods display significant disparities in Hausdorff distance in comparison to the ROI-centered method.

To fortify our decision-making process, our analysis is extended to the effect on aorta size and dilation on the predictions. This segmentation provides insightful observations, particularly for Healthy and Large Aortic Aneurysms (AAOs). The AAo and DAo-centered method consistently demonstrates marked improvements in both Dice score and Hausdorff distance evaluations, emphasizing its robust performance even in patients with complex aortic geometry.

A pivotal issue with the ROI-centered method lies in its vulnerability to substantial variations in aorta size. When the dimensions of both the AAo and DAo exceed the confines of the ROI, the image experiences a two-step transformation: an initial zoom-out operation to achieve the desired size followed by a subsequent zoom-in to reintegrate it into the original image. Regrettably, these manipulations entail an information loss, resulting in a drop in segmentation accuracy.

The foremost objective we aim to achieve is an accurate estimation of the flow velocity within the ascending aorta. Notably, when examining all utilized methods, both mean absolute error (MAE) and mean squared error (MSE) exhibit lower values in the context of the ascending aorta as opposed to the descending aorta scenario. This might be linked to the lower blood flow in the descending aorta. Additionally, focusing on the ascending aorta, the AAo and DAo-centered approach is the sole method that stands out from the Vanilla method, demonstrating a significant distinction in contrast to the ROI-centered method. This

underscores the unique efficacy of the AAo and DAo-centered method in the ascending aorta context, with the potential to bring about meaningful advancements in predictive accuracy and clinical applications.

In our investigation into aorta segmentation methods, we delved into the impact of different MRI machine characteristics, specifically considering manufacturers and magnetic field strengths. Consistent with other findings, we found superior results for the AAo and DAo-centered method.

Of particular interest was the standout performance observed with GE Medical systems equipped with a magnetic field strength of 3 Tesla (3 T). This configuration consistently yielded the most accurate results in terms of aorta segmentation. The synergy between GE Medical's technology and the higher magnetic field strength appears to provide a favorable environment for capturing the intricate details of the aorta.

However, a crucial factor influencing our analysis is the uneven distribution of the test set. This disparity introduces potential biases that warrant caution when drawing broad conclusions. The promising results from GE Medical's 3 T systems serve as a guide, but the need for a more balanced dataset is evident to establish the reliability of these findings.

To further enhance our methodology, we explored the temporal dynamics of cine MRI sequences. Notably, the three methods investigated in this study treated individual images within the sequence as independent entities. In an effort to capture sequential information, we explored the implementation of Bidirectional Long Short-Term Memory (Bilstm) and 3D approaches. However, due to pragmatic constraints related to hyperparameter tuning and computational complexity, these investigations were not exhaustively pursued.

Given the satisfactory outcomes achieved with the AAo and DAo-centered method (average Dice around 0.97), this approach is slated for integration into the ARTFUN software. This decision is informed by its robustness, demonstrated improvements in aorta segmentation accuracy, and its potential to contribute valuable insights in clinical settings.

## 6 | Conclusion

Aortic stiffness stands as a major indicator of cardiovascular health, playing a pivotal role in disease diagnosis and patient prognoses. The challenge of accurately segmenting the aorta from 2D dynamic MRI images, typically involving time-consuming traditional image processing methods with operator subjectivity, highlights the need for innovative solutions. This thesis introduces a groundbreaking approach to automated aortic lumen segmentation from the challenging dynamic velocity-encoded 2D MRI images, the signal in such images is proportional to the blood flow velocities making it fade in the diastolic phases. Leveraging deep learning techniques, specifically the UNet++ architecture, this research presents a robust solution to this intricate problem.

The UNet++ architecture, renowned for its capacity to capture intricate details and excel in semantic segmentation tasks, forms the foundation of our model. By integrating skip and dense connections, the architecture efficiently extracts features across various scales. Multiple algorithmic strategies were developed and assessed, including a comprehensive UNet++ processing of the entire image, a second variant focusing on a ROI encompassing both the AAO and DAO, and two distinct UNet++ models processing independent ROIs corresponding to either AAO or DAO.

Through a series of rigorous experiments involving hyperparameter optimization and varied training configurations, the efficacy of the Vanilla method and the AAO and DAO-centered method in accurately segmenting the aorta from 2D dynamic MRI images was robustly demonstrated. Both methods exhibited compelling results, revealing Dice coefficients surpassing 0.97 and Hausdorff distances smaller than 2 pixels. This exceptional agreement between the model's predictions and the ground truth segmentations underscores the potential for accurate, automated aortic segmentation.

In the framework of this internship, I had the invaluable opportunity to attend a seminar on medical imaging at NeuroSpin and a conference by Yann Le Cun on the past, present, and future of AI. These experiences enriched my understanding of medical imaging frontiers and provided insights into the broader context of AI's trajectory.

In conclusion, this thesis presents a pioneering solution for aortic segmentation in 2D

dynamic MRI images, hinging on the potent UNet++ architecture. The model's promising outcomes offers clinicians accurate and fully automated aortic segmentation to accurately quantify geometry and blood flow characteristics in human central aorta, which is specifically subject to aging and diseases like hypertension and aneurysms. This innovation bears the potential to significantly enhance the diagnosis and treatment of cardiovascular disorders, ultimately advancing patient care and outcomes.

## Bibliography

- [1] Pytorch documentation. URL <https://pytorch.org/features/>. Accessed 7/11/2023.
- [2] Tensorflow documentation. URL <https://www.tensorflow.org/>. Accessed 7/11/2023.
- [3] Basic anatomy of the human heart. *Cardiology Associates of Michigan, P.C.*, 2019. URL <https://www.cardofmich.com/anatomy-human-heart-fun-facts/>.
- [4] Systolic vs. diastolic blood pressure. *AND Medical*, Accessed 7/3/2023. URL <https://medical.andonline.com/systolic-vs-diastolic-blood-pressure/>.
- [5] M. Abadi, P. Barham, J. Chen, Z. Chen, A. Davis, J. Dean, M. Devin, S. Ghemawat, G. Irving, M. Isard, M. Kudlur, J. Levenberg, R. Monga, S. Moore, D. G. Murray, B. Steiner, P. Tucker, V. Vasudevan, P. Warden, M. Wicke, Y. Yu, and X. Zheng. Tensorflow: A system for large-scale machine learning. page 265–283, 2016. doi: 10.5555/3026877.3026899.
- [6] P. Arbeláez, M. Maire, C. Fowlkes, and J. Malik. Contour detection and hierarchical image segmentation. *IEEE Transactions on Pattern Analysis and Machine Intelligence*, 33(5):898–916, 2011. doi: 10.1109/TPAMI.2010.161.
- [7] N. E. M. Association. Ps3.1 - introduction and overview. 2023. URL <https://www.dicomstandard.org/current>. Accessed 08/18/2023.
- [8] W. Bai, H. Suzuki, C. Qin, G. Tarroni, O. Oktay, P. M. Matthews, and D. Rueckert. Recurrent neural networks for aortic image sequence segmentation with sparse annotations. *MICCAI Society*, 2018.
- [9] S. Barocas and A. D. Selbst. Big data’s disparate impact. *California Law Review*, 104: 671, 2016.
- [10] Y. Bengio, P. Y. Simard, and P. Frasconi. Learning long-term dependencies with gradient descent is difficult. *IEEE transactions on neural networks*, 5(2):157–166, 1994. doi: 10.1109/72.279181.

- [11] J. G. Betts, K. A. Young, J. A. Wise, E. Johnson, B. Poe, D. H. Kruse, O. Korol, J. E. Johnson, M. Womble, and P. DeSaix. *Anatomy and physiology*. *OpenStax*, 2013.
- [12] L. Biasioli, E. Hann, E. Lukaschuk, V. Carapella, J. M. Paiva, N. Aung, J. J. Rayner, K. Werys, K. Fung, H. Puchta, M. M. Sanghvi, N. O. Moon, R. J. Thomson, K. E. Thomas, M. D. Robson, V. Grau, S. E. Petersen, S. Neubauer, and S. K. Piechnik. Automated localization and quality control of the aorta in cine cmr can significantly accelerate processing of the uk biobank population data. *PlosOne*, 2019.
- [13] P. Bickel and K. Doksum. *Mathematical Statistics: Basic Ideas and Selected Topics*, volume 56. 2007. doi: 10.2307/2286373.
- [14] C. Bodnar. *Text to Image Synthesis Using Generative Adversarial Networks*. PhD thesis, 04 2018.
- [15] P. Boutouyrie, A. I. Tropeano, R. Asmar, I. Gautier, A. Benetos, P. Lacolley, and S. Laurent. Aortic stiffness is an independent predictor of primary coronary events in hypertensive patients: a longitudinal study. *Hypertension*, 2002. doi: 10.1161/hy0102.099031.
- [16] J. Budde, G. Shajan, J. Hoffmann, K. Uğurbil, and R. Pohmann. Human imaging at 9.4 t using t2\*- , phase-, and susceptibility-weighted contrast. *Magnetic resonance in medicine*, 65(2):544–550, 2011.
- [17] J. Buolamwini and T. Gebru. Gender shades: Intersectional accuracy disparities in commercial gender classification. In S. A. Friedler and C. Wilson, editors, *Proceedings of the 1st Conference on Fairness, Accountability and Transparency*, volume 81 of *Proceedings of Machine Learning Research*, pages 77–91. PMLR, 2018.
- [18] P. Chai and R. Mohiaddin. How we perform cardiovascular magnetic resonance flow assessment using phase-contrast velocity mapping. *Journal of cardiovascular magnetic resonance : official journal of the Society for Cardiovascular Magnetic Resonance*, 7:705–16, 02 2005. doi: 10.1081/JCMR-65639.
- [19] O. Cicek, A. Abdulkadir, S. S. Lienkamp, T. Brox, and O. Ronneberger. 3d u-net: Learning dense volumetric segmentation from sparse annotation. *International Conference on Medical Image Computing and Computer-Assisted Intervention*, pages 424–432, 2016.
- [20] M. Clinic. Mri. URL <https://www.mayoclinic.org/tests-procedures/mri/about/pac-20384768>. Accessed 6/20/2023.

- [21] S. Costantino, F. Paneni, and F. Cosentino. Ageing, metabolism and cardiovascular disease. *The Journal of Physiology*, 595(8):2061–2073, 2016. doi: 10.1113/JP270538.
- [22] T. M. Cover and J. A. Thomas. *Elements of Information Theory 2nd Edition (Wiley Series in Telecommunications and Signal Processing)*. Wiley-Interscience, 2006.
- [23] L. R. Dice. Measures of the amount of ecologic association between species. *Ecology*, 26(3):297–302, 1945. doi: 10.2307/1932409.
- [24] A. Dogui, N. Kachenoura, F. Frouin, M. Lefort, A. De Cesare, E. Mousseaux, and A. Herment. Consistency of aortic distensibility and pulse wave velocity estimates with respect to the bramwell-hill theoretical model: a cardiovascular magnetic resonance study. *JCMR*, 2011.
- [25] A. Dogui, A. Redheuil, M. Lefort, A. De Cesare, N. Kachenoura, A. Herment, and E. Mousseaux. Measurement of aortic arch pulse wave velocity in cardiovascular mr: Comparison of transit time estimators and description of a new approach. *JMRI*, 2011.
- [26] M. P. Dubuisson and A. K. Jain. A modified hausdorff distance for object matching. *Proceedings of the 12th IAPR International Conference on Pattern Recognition*, 1:566–568, 1994. doi: 10.1109/ICPR.1994.576361.
- [27] O. M. F. The arterial pulse in health and disease. *Am Heart J*, 82(5):687–702, 1972. doi: 10.1016/0002-8703(71)90340-1.
- [28] J. Feger, A. Murphy, and D. Bell. Cine imaging (mri). *Radiopaedia*, 2023. doi: 10.53347/rID-80651. URL <https://radiopaedia.org/articles/80651>. Accessed 08/21/2023.
- [29] H. Foundation. How the heart works. *Heart Foundation*, Accessed 7/3/2023. URL <https://www.heartfoundation.org.nz/your-heart/how-the-heart-works>.
- [30] S. S. Franklin, S. A. Khan, N. D. Wong, M. G. Larson, and D. Levy. Is pulse pressure useful in predicting risk for coronary heart disease? *The Framingham Heart Study*, 1999. doi: 10.1161/01.cir.100.4.354.
- [31] S. Glüge, R. Böck, G. Palm, and A. Wendemuth. Learning long-term dependencies in segmented-memory recurrent neural networks with backpropagation of error. *Neuro-computing*, 141:54–64, 2014. doi: <https://doi.org/10.1016/j.neucom.2013.11.043>.
- [32] I. J. Good. Maximum entropy for hypothesis formulation, especially for multidimensional contingency tables. *Annals of Mathematical Statistics*, 34:911–934, 1963.
- [33] I. Goodfellow, Y. Bengio, and A. Courville. Deep learning. *MIT Press*, 2016.

- [34] A. Graves. Generating sequences with recurrent neural networks. *CoRR*, 2013. URL <http://arxiv.org/abs/1308.0850>.
- [35] E. Hann, L. Biasioli, Q. Zhang, I. A. Popescu, K. Werys, E. Lukaschuk, V. Carapella, J. M. Paiva, N. Aung, J. J. Rayner, K. Fung, H. Puchta, M. M. Sanghvi, N. O. Moon, K. E. Thomas, V. M. Ferreira, S. E. Petersen, S. Neubauer, and S. K. Piechnik. Quality control-driven image segmentation towards reliable automatic image analysis in large-scale cardiovascular magnetic resonance aortic cine imaging. *MICCAI Society*, 2019.
- [36] F. Hausdorff. Grundzüge der mengenlehre (= basics of set theory). pages 116–129, 1914.
- [37] K. He, X. Zhang, S. Ren, and J. Sun. Deep residual learning for image recognition. 2015. doi: 10.1109/CVPR.2016.90.
- [38] A. Herment, N. Kachenoura, M. Lefort, M. Bensalah, A. Dogui, F. Frouin, E. Mousseaux, and A. De Cesare. Automated segmentation of the aorta from phase contrast mr images: Validation against expert tracing in healthy volunteers and in patients with a dilated aorta. *JMRI*, 2010.
- [39] A. T. Hess, M. M. Bissell, N. A. Ntusi, A. J. Lewis, E. M. Tunnicliffe, A. Greiser, A. F. Stalder, J. M. Francis, S. G. Myerson, S. Neubauer, and M. D. Robson. Aortic 4d flow: Quantification of signal-to-noise ratio as a function of field strength and contrast enhancement for 1.5t, 3t, and 7t. *Magnetic Resonance in Medicine*, 73(5):1864–1871, 2015. doi: 10.1002/mrm.25317.
- [40] S. Hochreiter and J. Schmidhuber. Long Short-Term Memory. *Neural Computation*, 9(8):1735–1780, 1997. doi: 10.1162/neco.1997.9.8.1735.
- [41] T. M. Ingolfsson. Insights into lstm architecture. 2021. URL [https://thorirmar.com/post/insight\\_into\\_lstm/](https://thorirmar.com/post/insight_into_lstm/). Accessed 8/06/2023.
- [42] A. Karpathy. The unreasonable effectiveness of recurrent neural networks. 2015. URL <http://karpathy.github.io/2015/05/21/rnn-effectiveness/>. Accessed 8/02/2023.
- [43] J. Kim and J. Kim. Bilstm model based on multivariate time series data in multiple field for forecasting trading area. *Journal of Ambient Intelligence and Humanized Computing*, 07 2019. doi: 10.1007/s12652-019-01398-9.
- [44] D. P. Kingma and J. Ba. Adam: A method for stochastic optimization. *Cornell University - arXiv*, 2017. doi: 10.48550/arxiv.1412.6980.

- [45] A. Krizhevsky and G. Hinton. Learning multiple layers of features from tiny images. Technical Report 0, University of Toronto, Toronto, Ontario, 2009.
- [46] A. Krizhevsky, I. Sutskever, and G. Hinton. Imagenet classification with deep convolutional neural networks. *Neural Information Processing Systems*, 2012. doi: 10.1145/3065386.
- [47] A. Kumar, D. J. Patton, and M. G. Friedrich. The emerging clinical role of cardiovascular magnetic resonance imaging. *Can J Cardiol*, 26(6):313–322, 2010. doi: 10.1016/s0828-282x(10)70396-2.
- [48] S. Laurent, P. Boutouyrie, R. Asmar, I. Gautier, B. Laloux, L. Guize, P. Ducimetiere, and A. Benetos. Aortic stiffness is an independent predictor of all-cause and cardiovascular mortality in hypertensive patients. *Hypertension*, 2001. doi: 10.1161/01.hyp.37.5.1236.
- [49] S. Laurent, P. Boutouyrie, and P. Lacolley. Structural and genetic bases of arterial stiffness. *Hypertension*, 45(6):1050–1055, 2005. doi: 10.1161/01.HYP.0000164580.39991.3d.
- [50] C. Le Ster, A. Grant, P. Van de Moortele, A. Monreal-Madrigal, G. Adriany, A. Vignaud, F. Mauconduit, C. Rabrait-Lerman, B. A. Poser, K. Uğurbil, and N. Boulant. Magnetic field strength dependent snr gain at the center of a spherical phantom and up to 11.7t. *Magnetic resonance in medicine*, 88(5):2131–2138, 2022.
- [51] Y. LeCun, Y. Bengio, and G. Hinton. Deep learning. *Nature*, 2015. doi: 10.1038/nature14539.
- [52] J. Ma. Segmentation loss odyssey. 2020. doi: 10.48550/arXiv.2005.13449.
- [53] M. Markl, A. Frydrychowicz, S. Kozerke, M. Hope, and O. Wieben. 4d flow mri. *Journal of Magnetic Resonance Imaging*, 36(5):1015–1036, 2012. doi: 10.1002/jmri.23632.
- [54] C. H. McDonnell, R. J. Herfkens, A. M. Norbash, and G. D. Rubin. Magnetic resonance imaging and measurement of blood flow. *The Western journal of medicine*, 160(3): 237–242, 1994. PMID: 8191756.
- [55] S. Medicine. Pet/mri scan. *Stanford Medicine Health Care*. URL <https://stanfordhealthcare.org/medical-tests/p/pet-mri-scan.html>. Accessed 7/7/2023.
- [56] F. Milletari, N. Navab, and S.-A. Ahmadi. V-net: Fully convolutional neural networks

- for volumetric medical image segmentation. pages 565–571, 2016. doi: 10.1109/3DV.2016.79.
- [57] G. M. Miranda. Structure and function of the heart. *News-Medical*, 2022, Accessed 7/3/2023. URL <https://www.news-medical.net/health/Structure-and-Function-of-the-Heart.aspx>.
- [58] T. Miyoshi and H. Ito. Arterial stiffness in health and disease: The role of cardio-ankle vascular index. *Journal of Cardiology*, 78(6):493–501, 2021. ISSN 0914-5087. doi: <https://doi.org/10.1016/j.jjcc.2021.07.011>. URL <https://www.sciencedirect.com/science/article/pii/S0914508721001945>.
- [59] K. S. Nayak, J. F. Nielsen, M. A. Bernstein, M. Markl, P. D. Gatehouse, R. M. Botnar, D. Saloner, C. Lorenz, H. Wen, B. S. Hu, F. H. Epstein, J. N. Oshinski, and S. V. Raman. Cardiovascular magnetic resonance phase contrast imaging. *Journal of cardiovascular magnetic resonance : official journal of the Society for Cardiovascular Magnetic Resonance*, 17(1):71, 2015. doi: 10.1186/s12968-015-0172-7.
- [60] M. Nikpanah, W. R. Willoughby, A. E. Campbell-Washburn, J. T. S. Denney, A. A. Malayeri, L. ver Hoef, and K. K. Porter. Low versus ultra-high field mri: How to select your mri fleet. *Applied Radiology*, 2023. URL <https://appliedradiology.com/articles/low-versus-ultra-high-field-mri-how-to-select-your-mri-fleet#>. Accessed 7/12/2023.
- [61] N. I. of Biomedical Imaging and Bioengineering. Magnetic resonance imaging (mri). *National Institutes of Health*. URL <https://www.nibib.nih.gov/science-education/science-topics/magnetic-resonance-imaging-mri>. Accessed 6/22/2023.
- [62] S. Ohtsuka, M. Kakihana, H. Watanabe, and Y. Sugishita. Chronically decreased aortic distensibility causes deterioration of coronary perfusion during increased left ventricular contraction. *J Am Coll Cardiol*, 1994. doi: 10.1016/0735-1097(94)90127-9.
- [63] W. H. Organization. Global atlas on cardiovascular disease prevention and control. 2011. URL <https://www.who.int/publications/i/item/9789241564373>.
- [64] C. Palombo and M. Kozakova. Arterial stiffness, atherosclerosis and cardiovascular risk: Pathophysiologic mechanisms and emerging clinical indications. *Vascul Pharmacol*, 2016. doi: 10.1016/j.vph.2015.11.083.
- [65] A. Paszke, S. Gross, F. Massa, A. Lerer, J. Bradbury, G. Chanan, T. Killeen, Z. Lin,

- N. Gimelshein, L. Antiga, A. Desmaison, A. Kopf, E. Yang, Z. DeVito, M. Raison, A. Tejani, S. Chilamkurthy, B. Steiner, L. Fang, J. Bai, and S. Chintala. Pytorch: An imperative style, high-performance deep learning library. **32**, 2019.
- [66] J. D. Pollock and A. N. Makaryus. Physiology, cardiac cycle. *National Library of Medicine*, 2023. URL <https://www.ncbi.nlm.nih.gov/books/NBK459327/>.
- [67] R. Qayyum. Introduction to pooling layers in cnn. *Towards AI*, 2022. URL <https://pub.towardsai.net/introduction-to-pooling-layers-in-cnn-dafe61eabe34>. Accessed 7/11/2023.
- [68] RadiologyInfo. Body mri. 2022. URL <https://www.radiologyinfo.org/en/info/bodymr>. Accessed 7/5/2023.
- [69] A. Rajkomar, E. Oren, K. Chen, A. Dai, N. Hajaj, P. Liu, X. Liu, M. Sun, P. Sundberg, H. Yee, K. Zhang, G. Duggan, G. Flores, M. Hardt, J. Irvine, Q. Le, K. Litsch, J. Marcus, A. Mossin, and J. Dean. Scalable and accurate deep learning for electronic health records. *npj Digital Medicine*, 1, 2018. doi: 10.1038/s41746-018-0029-1.
- [70] S. V. Ramachandran. Pathogenesis of elevated peripheral pulse pressure. *AHA*, 51: 33–36, 2008. doi: 10.1161/HYPERTENSIONAHA.107.101196.
- [71] Rocchini. Hausdorff distance — Wikipedia, the free encyclopedia, 2023. URL [https://en.wikipedia.org/w/index.php?title=Hausdorff\\_distance&oldid=1162505883](https://en.wikipedia.org/w/index.php?title=Hausdorff_distance&oldid=1162505883). Accessed 7/4/2023.
- [72] O. Ronneberger, P. Fischer, and T. Brox. U-net: Convolutional networks for biomedical image segmentation. *International Conference on Medical Image Computing and Computer-Assisted Intervention*, pages 234–241, 2015.
- [73] V. M. Runge and J. T. Heverhagen. The clinical utility of magnetic resonance imaging according to field strength, specifically addressing the breadth of current state-of-the-art systems, which include 0.55 t, 1.5 t, 3 t, and 7 t. *Investigative Radiology*, 57(1):1–12, 2022. doi: 10.1097/RLI.0000000000000824.
- [74] W. Samek, T. Wiegand, and K.-R. Müller. Explainable artificial intelligence: Understanding, visualizing and interpreting deep learning models. *ITU Journal: ICT Discoveries - Special Issue 1 - The Impact of Artificial Intelligence (AI) on Communication Networks and Services*, 1:1–10, 2017.
- [75] S.-L. Shen, P. G. Atangana Njock, A. Zhou, and H.-M. Lyu. Dynamic prediction of jet grouted column diameter in soft soil using bi-lstm deep learning. *Acta Geotechnica*, 16, 2021. doi: 10.1007/s11440-020-01005-8.

- [76] S. Siami-Namini, N. Tavakoli, and A. S. Namin. The performance of lstm and bilstm in forecasting time series. In *2019 IEEE International Conference on Big Data (Big Data)*, pages 3285–3292, 2019. doi: 10.1109/BigData47090.2019.9005997.
- [77] N. Siddique, S. Paheding, C. P. Elkin, and V. Devabhaktuni. U-net and its variants for medical image segmentation: A review of theory and applications. *IEEE Access*, 9: 82031–82057, 2021. doi: 10.1109/ACCESS.2021.3086020.
- [78] K. Simonyan and A. Zisserman. Very deep convolutional networks for large-scale image recognition, 2015.
- [79] T. Sorensen. A method of establishing groups of equal amplitude in plant sociology based on similarity of species content and its application to analyses of the vegetation on danish commons. *Biologiske Skrifter/Kongelige Danske Videnskabernes Selskab*, 5:1–34, 1948.
- [80] L. N. Tanenbaum. Clinical 3t mr imaging: mastering the challenges. *Magnetic resonance imaging clinics of North America*, 14(1):1–15, 2006. doi: 10.1016/j.mric.2005.12.004.
- [81] C. Triantafyllou, R. Hoge, G. Krueger, C. Wiggins, A. Potthast, G. Wiggins, and L. Wald. Comparison of physiological noise at 1.5 t, 3 t and 7 t and optimization of fmri acquisition parameters. *NeuroImage*, 26(1):243–250, 2005. doi: <https://doi.org/10.1016/j.neuroimage.2005.01.007>.
- [82] K. Ugurbil. Magnetic resonance imaging at ultrahigh field. *IEEE transactions on bio-medical engineering*, 61(5):1364–1379, 2014. doi: 10.1109/TBME.2014.2313619.
- [83] M. J. van Hout, A. J. Scholte, J. F. Juffermans, J. J. Westenberg, L. Zhong, X. Zhou, S. M. Schalla, M. D. Hope, J. Bremerich, C. M. Kramer, M. Dewey, K. G. Orдовas, D. A. Bluemke, and H. J. Lamb. How to measure the aorta using mri: A practical guide. *JMRI*, 2020.
- [84] F. L. J. Visseren, F. Mach, Y. M. Smulders, D. Carballo, K. C. Koskinas, M. Bäck, A. Benetos, A. Biffi, J.-M. Boavida, D. Capodanno, B. Cosyns, C. Crawford, C. H. Davos, I. Desormais, E. Di Angelantonio, O. H. Franco, S. Halvorsen, F. D. R. Hobbs, M. Hollander, E. A. Jankowska, M. Michal, S. Sacco, N. Sattar, L. Tokgozoglu, S. Tonstad, K. P. Tsioufis, I. van Dis, I. C. van Gelder, C. Wanner, B. Williams, and E. S. D. Group. 2021 esc guidelines on cardiovascular disease prevention in clinical practice: Developed by the task force for cardiovascular disease prevention in clinical practice with representatives of the european society of cardiology and 12 medical societies with the special contribution of the european association of

- preventive cardiology (eapc). *European Heart Journal*, 42(34):3227–3337, 2021. doi: 10.1093/eurheartj/ehab484.
- [85] C. Vlachopoulos, M. O’Rourke, and W. W. Nichols. *McDonald’s Blood Flow in Arteries: Theoretical, Experimental and Clinical Principles*. CRC Press, 6 edition, 2012. ISBN 9780429166921. doi: 10.1201/b13568. Chapter 9.
- [86] C. Willmott and K. Matsuura. Advantages of the mean absolute error (mae) over the root mean square error (rmse) in assessing average model performance. *Climate Research*, 30:79, 2005. doi: 10.3354/cr030079.
- [87] C. F. Wu, P. Y. Liu, T. J. Wu, Y. Hung, S. P. Yang, and G. M. Lin. Therapeutic modification of arterial stiffness: An update and comprehensive review. *World J Cardiol*, 2015. doi: 10.4330/wjc.v7.i11.742.
- [88] J. Yosinski, J. Clune, Y. Bengio, and H. Lipson. How transferable are features in deep neural networks? *Advances in Neural Information Processing Systems (NIPS)*, 27, 11 2014.
- [89] L. Zanolini, P. Lentini, M. Briet, P. Castellino, A. A. House, G. M. London, L. Malatino, P. A. McCullough, D. P. Mikhailidis, and P. Boutouyrie. Arterial stiffness in the heart disease of ckd. *J Am Soc Nephrol*, 2019. doi: 10.1681/ASN.2019020117.
- [90] M. Zheng, X. Zhang, S. Chen, Y. Song, Q. Zhao, X. Gao, and S. Wu. Arterial stiffness preceding diabetes. *A Longitudinal Study*, 2020. doi: 10.1161/CIRCRESAHA.120.317950.
- [91] Z. Zhou, M. M. R. Siddiquee, N. Tajbakhsh, and J. Liang. Unet++: A nested u-net architecture for medical image segmentation. *MICCAI*, 2018. doi: 10.1007/978-3-030-00889-5\_1.
- [92] J. Zhuang. Laddernet: Multi-path networks based on u-net for medical image segmentation. *CoRR*, abs/1810.07810, 2018.
- [93] V. Zyuzin and T. Chumarnaya. Comparison of unet architectures for segmentation of the left ventricle endocardial border on two-dimensional ultrasound images. pages 110–113, 2019. doi: 10.1109/USBREIT.2019.8736616.



## List of Figures

1.1	Distribution of global NCD by causes of deaths . . . . .	2
1.2	Heart anatomy Scheme . . . . .	3
1.3	Systole and Diastole Schemes . . . . .	4
1.4	Aorta . . . . .	5
1.5	Reflected wave of the aorta . . . . .	6
1.6	MRI Machine . . . . .	8
1.7	Phase Contrast cine MRI . . . . .	10
1.8	Aortic Stiffness Representation . . . . .	12
1.9	Reflected wave of the stiffened aorta . . . . .	13
2.1	Ultra-High Field MRI . . . . .	19
2.2	Stride and padding . . . . .	21
2.3	Max Pooling and Average Pooling . . . . .	22
2.4	UNet architecture . . . . .	26
2.5	UNet++ Schema . . . . .	28
2.6	Recurrent Neural Network Interactions Schema . . . . .	29
2.7	LSTM cell architecture . . . . .	30
2.8	LSTM and BiLSTM schema . . . . .	32
2.9	Biasiolli et al. method . . . . .	33
2.10	Bai et al. method . . . . .	34
2.11	Hann et al. method . . . . .	35
3.1	DICOM Metadata example . . . . .	38
3.2	Modulus, Velocity and Groundtruth of a cine MRI . . . . .	39
3.3	Dataset Split . . . . .	42
3.4	ROI-centered Method Schema . . . . .	44
3.5	AAo and DAo-centered method Schema . . . . .	45
3.6	Dice Representation . . . . .	48
3.7	Hausdorff Representation . . . . .	49
4.1	Results on the whole test set - Dice Score . . . . .	52

4.2	Wilcoxon Significance computation Dice AAO . . . . .	52
4.3	Wilcoxon Significance computation Dice DAo . . . . .	53
4.4	Results on the whole test set - Hausdorff distance . . . . .	53
4.5	Wilcoxon Significance computation Hausdorff AAO . . . . .	53
4.6	Wilcoxon Significance computation Hausdorff DAo . . . . .	54
4.7	Aortic Size Comparison - AAO Dice Score . . . . .	56
4.8	Aortic Size Comparison - DAo Dice Score . . . . .	57
4.9	Aortic Size Comparison - AAO Hausdorff distance . . . . .	58
4.10	Aortic Size Comparison - DAo Hausdorff distance . . . . .	59
4.11	Blood flow velocity Accuracy Comparison - Mean Absolute Error . . . . .	60
4.12	Wilcoxon Significance computation MAE Velocity AAO . . . . .	60
4.13	Wilcoxon Significance computation MAE Velocity DAo . . . . .	61
4.14	Blood flow velocity Accuracy Comparison - Mean Squared Error . . . . .	62
4.15	Wilcoxon Significance computation MSE Velocity AAO . . . . .	62
4.16	Wilcoxon Significance computation MSE Velocity DAo . . . . .	62

## List of Tables

4.1	Results on the whole test set . . . . .	52
4.2	State of the Art Dice Score comparison . . . . .	54
4.3	Aortic Size Comparison - AAo Dice Score . . . . .	55
4.4	Aortic Size Comparison - DAo Dice Score . . . . .	56
4.5	Aortic Size Comparison - AAo Hausdorff distance . . . . .	57
4.6	Aortic Size Comparison - DAo Hausdorff distance . . . . .	58
4.7	Blood flow velocity Accuracy Comparison - Mean Absolute Error . . . . .	60
4.8	Blood flow velocity Accuracy Comparison - Mean Squared Error . . . . .	61
4.9	MRI Machines Comparison - Test Set Distribution . . . . .	63
4.10	MRI Machines Comparison - AAo Dice score . . . . .	64
4.11	MRI Machines Comparison - DAo Dice score . . . . .	64



## Acronyms

**AAo** Ascending Aorta

**ARTFUN** ARTerial FUNction

**BiLSTM** Bidirectional Long Short-Term Memory

**CNN** Convolutional Neural Network

**CT** Computed Tomography

**CVD** Cardiovascular Diseases

**DAo** Descending Aorta

**DL** Deep Learning

**DSC** Dice Similarity Coefficient

**LIB** Laboratoire d'Imagerie Biomédicale

**LSTM** Long Short-Term Memory

**MAE** Mean Absolute Error

**MRI** Magnetic Resonance Imaging

**MSE** Mean Squared Error

**NCD** Noncommunicable Diseases

**PC** Phase Contrast

**PWV** Pulse Wave Velocity

**ReLU** Rectified Linear Unit

**RF** Random Forest

**RM** Risonanza Magnetica

**RNN** Recurrent Neural Networks

**ROI** regione d'interesse

**ROI** Region of Interest

**WHO** World Health Organization

## Acknowledgements

I would like to express my deepest gratitude and appreciation to the Politecnico di Milano for providing me with the opportunity to pursue my academic journey. The support and resources offered by this esteemed institution have been instrumental in shaping my intellectual growth and enabling me to undertake this thesis. I am particularly indebted to my university advisor, Professor Elena De Momi, for her guidance and expertise throughout this research endeavor.

I would also like to extend my heartfelt thanks to my advisors, Lecturer Thomas Dietenbeck and Research Director Nadja Kachenoura, for their valuable contributions, mentorship, and profound knowledge in their respective fields. Their expertise has broadened my horizons, inspired critical thinking, and enriched the depth of my research.

I wish to express my sincere appreciation to the medical staff who participated in the meticulous segmentation of the images, which served as the groundtruth for training our model. Their collaboration has been instrumental in the success of this study.

Additionally, I would like to acknowledge the collaborative efforts of my coworkers from the Laboratoire d'Imagerie Biomédicale in the ICV section. Their constant support, insightful discussions, and diverse perspectives have significantly influenced the development and outcome of this thesis. Their contributions have not only enhanced my understanding but also fostered an environment of growth and learning.

Finally, I would like to express my deepest gratitude to all my friends and family members who have provided unwavering support, encouragement, and understanding throughout this academic journey. Their love, patience, and belief in my abilities have been an immense source of motivation and strength.

To all those mentioned above and to many others who have played a part in my academic and personal development, I want to say a heartfelt thank you. This thesis would not have been possible without your support and belief in me.

